

Pore-scale modeling of deformation and shear band bifurcation in porous crystalline rocks

Martin Tjioe and Ronaldo I. Borja^{*,†}

Department of Civil and Environmental Engineering, Stanford University, Stanford, CA 94305, USA.

SUMMARY

We develop a computational framework that captures the microfracture processes leading to shear band bifurcation in porous crystalline rocks. The framework consists of computational homogenization on a representative elementary volume that upscales the pore-scale microfracture processes to the continuum scale. The assumed enhanced strain finite element approach is used to capture the discontinuous displacement field generated by the microfractures. Homogenization at the continuum scale results in incrementally nonlinear material response, in which the overall constitutive tangent tensor varies with the stress state and with the loading direction. Continuum bifurcation detects the formation of a shear band on the representative elementary volume level; multi-dimensional strain probes, necessitated by the incremental nonlinearity of the overall constitutive response, determine the most critical orientation of shear band bifurcation. Numerical simulations focus on microfracturing at the pore scale with either predominant interface separation or predominant interface contact modes. Results suggest a non-associative overall plastic flow and shear band bifurcation that depends on the microfracture length and the characteristic sliding distance related to slip weakening. Copyright © 2016 John Wiley & Sons, Ltd.

Received 27 February 2015; Revised 30 December 2015; Accepted 5 January 2016

KEY WORDS: crystal plasticity; heterogeneity; homogenization; incremental nonlinearity; microfracture; pore-scale mechanism

1. INTRODUCTION

Strain localization is a ubiquitous feature of deformation in geomaterials. Typical manifestations include deformation bands, which are narrow tabular zones of intense shearing often accompanied by compaction or dilation [1, 2]. Classic continuum bifurcation theory is commonly used to predict the inception of a deformation band. However, bifurcation analyses are known to be strongly dependent on the constitutive tangent tensor, where small perturbations could significantly alter the predicted timing and mode of bifurcation [3]. Because the constitutive tensor is a gross approximation of more complex multiscale deformation processes occurring at a much smaller pore scale, results of shear band bifurcation are normally met with skepticisms particularly for geomaterials (soils and rocks) where constitutive models are usually developed from laboratory responses of large bulk samples [4–7] and do not consider the effect of heterogeneity at smaller scales [8–16].

Pore-scale mechanisms play a key role in carbon sequestration, hydraulic fracturing, and enhanced hydrocarbon recovery activities that have long been suspected of triggering seismicity and fault rupture/propagation [17–28]. In rocks, crystal plasticity and microfracturing are two dominant pore-scale mechanisms of deformation. Crystal plasticity generally results in a more ductile overall stress–strain response, whereas microfracturing leads to a more brittle response. Whatever the process, damage typically nucleates at the periphery of the voids and propagates into the interior

^{*}Correspondence to: Ronaldo I. Borja, Department of Civil and Environmental Engineering, Stanford University, Stanford, CA 94305, USA.

[†]E-mail: borja@stanford.edu

of the solid [29, 30]. The presence of adjacent voids tends to intensify damage as plastic and/or microfracture zones coalesce and produce much larger damage zones. All of these complex pore-scale mechanisms could impact the prediction of shear band bifurcation on the continuum scale; unfortunately, they are not represented adequately in most phenomenological constitutive models. In this paper, we focus on the microfracture processes at the pore scale, which trigger shear band bifurcation in crystalline rocks.

An important aspect of shear band bifurcation, largely ignored in previous work, concerns the issue of incremental nonlinearity [31–34]. In an incrementally nonlinear solid, the constitutive tangential moduli vary not only with the stress state but also with the stress or strain perturbation. An example of an incrementally nonlinear solid is a simple elastoplastic solid: unloading and loading perturbations can lead to two different mechanical responses, namely, elastic response and plastic response. Thus, two different branches of the tangent constitutive tensor can be expected: an elastic branch and a plastic branch. However, when the inelastic response is dominated by microfracture processes, even a loading perturbation can trigger multiple branches of the tangent constitutive tensor depending on the microfractures activated by the perturbation. In this case, it is essential to conduct stress (or strain) probing to determine which branch of the constitutive tensor defines the most critical mode of bifurcation.

Laboratory experiments have been conducted in the past to investigate the inelastic response of geomaterials using a large number of laboratory stress probes, such as those conducted by Anandarajah [35] on Ottawa sand and Royis and Doanh [36] on Hostun sand. Their experiments, however, contain stringent requirements on the setup procedure that are very difficult to achieve. With the inelastic deformation as the key output of the investigation, the same sample cannot be used in more than one loading schedule because the microstructure is altered at the end of each experiment. As such, identical samples have to be obtained for each test, which cannot be realistically performed in practice. Numerical simulations are used as an alternative to circumvent the problems encountered with laboratory experiments. The advantage of using numerical models is that identical ‘samples’ can be obtained easily and subjected to a series of probes. Despite concerns that the various simplifying assumptions employed in the numerical models may cause the results to deviate from the actual behavior of real samples, numerical models still offer great insights into phenomena that could not be investigated experimentally.

The discrete element method (DEM) [11, 37, 38] is commonly used to investigate the incremental response of granular materials. Bardet [39] conducted stress probes on a two-dimensional (2D) DEM model consisting of random assemblies of rigid and weightless circular disks. The incremental responses from the limited number of probes suggested that idealized granular materials showed incrementally piecewise-linear behavior as described by a single-mechanism non-associative elastoplasticity. Kishino [40] and Calvetti *et al.* [32] subjected three-dimensional (3D) DEM models with spherical particles to greater range of probing paths and more complex initial state and showed that single-mechanism elastoplasticity was insufficient in describing the incremental behavior of granular materials. Alonso-Marroquín and Herrmann [41] used assemblies of 2D polygonal particles and compared the accuracy of elastoplasticity theory with two tensorial zones and hypoplasticity theory in describing the incremental response. Froiio and Roux [42] used a 2D DEM model and applied stress probes in 3D stress space that included stress increment with principal axis rotation (shear). Recent work by Andrade *et al.* [43] with non-uniform rational basis spline (NURBS) has attempted to capture 3D grain shapes more realistically. In general, however, DEM-based solutions are not appropriate for simulating the nucleation and development of microfractures as trigger of deformation bands because they rely on an already discrete assembly even before the loading process begins.

This paper takes on a different approach for simulating the nucleation, growth, and coalescence of microfractures as they impact the triggering of a shear band in a porous crystalline rock. The proposed approach combines strong-discontinuity finite elements, computational homogenization on the representative elementary volume (REV) level, and shear band bifurcation analysis with 3D probing to check the onset of a shear band in an incrementally nonlinear material. The first ingredient of the approach, which of strong-discontinuity finite element modeling, has been presented in a recent paper by Tjioe and Borja [30]. In this approach, microfractures are inserted into the finite

elements in the form of a strong discontinuity, or displacement jump, according to the strength and geometric properties of the crystal. Unlike most previous work in strong discontinuity, no attempt is made to ‘connect’ activated displacement jumps into one single fracture or crack; instead, microfractures simply soften this element in the direction of the displacement jump. Therefore, ‘microfracture coalescence’ may be defined loosely in the context of a group of adjacent finite elements softened by the strong discontinuity, and no tracking of the discontinuity is required by the proposed approach. More recently, several other alternative variations by which strong discontinuity can be embedded into a finite element have been proposed to simulate damage [44–48].

The second ingredient of the approach, namely, computational homogenization, is performed on the REV level and entails an explicit treatment of the voids and crystal orientation as part of the material microstructure. The algorithm for homogenization is similar to that proposed by Miehe and Koch [49], where homogeneous deformation is applied on the boundary of the REV, and the homogenized stresses and tangent constitutive tensors are evaluated over the volume of the REV. The third ingredient consists of a full bifurcation analysis with strain probing where the entire range of possible bifurcation modes is checked and the most critical mode is selected. The numerical model is used to investigate the incremental responses of rocks and to answer the following questions pertaining to bifurcation: (1) Is a single-mechanism elastoplasticity sufficient to describe the incremental responses of rocks? (2) Can the homogenized response of the REV be used to detect the occurrence of bifurcation? (3) What overall incremental behavior can be expected when the microfractures are predominantly of the interface separation as opposed to contact mode?

Throughout this paper, the following notations and symbols are used: boldface letters denote tensors and matrices, and subscripted letters denote their scalar components. The summation convention is not enforced in this paper. We follow the standard engineering mechanics convention in which compression takes on a negative sign. All formulations are based on infinitesimal strain.

2. METHODOLOGY

The computational model takes into account the crystalline structure of a rock by recognizing that slip can occur on any of the slip planes within the crystal lattice. Using the algorithm developed in [50–52] and focusing on the infinitesimal range, the primary slip system is identified from the possibly dependent and potentially active constraints representing slip events on the crystallographic glide planes. The normal to the slip plane and direction of the primary slip system subsequently characterize the immediately developed microfractures, which are modeled using the assumed enhanced strain (AES) or strong-discontinuity finite element method [53–65]. Slip that occurs on the surface of the microfracture ensures that shear stress is balanced by shear resistance (comprising friction and/or cohesion) and that normal stress vanishes for interface separation. We emphasize that the microfractures considered in this work pertain to random, discontinuous cracks and not to a continuous crack that requires a special tracking algorithm [30]. This ensures a separation of scales — the REV homogenizes the smaller scale constitutive responses, whereas the macrofractures are tracked from one REV to another, although this latter aspect is not covered in the present paper.

2.1. Interface separation and contact

Upon the formation of a microfracture, slip weakening takes place where the cohesion on the surface decreases with slip magnitude and the contact condition for shear contact transitions into a purely frictional behavior. This occurs over a characteristic sliding distance ζ^+ . The surface constitutive behavior differs in the case of normal separation and shear contact.

For normal separation, the frictional resistance is nonexistent. The interfaces are free to slip in any tangential directions along the plane of the interface and in the direction normal to the plane. The stress on the interface eventually drops to zero over the separation distance ζ^+ . This results in a total of three interface yield conditions on the microfractured finite element e ,

$$f_{t1}^e = |\tau_1^e| - c_1^e = 0 \quad (1)$$

$$f_{t2}^e = |\tau_2^e| - c_2^e = 0 \quad (2)$$

$$f_n^e = \sigma^e - b^e = 0, \quad (3)$$

where c_1^e , c_2^e , and b^e are weakening laws of the form

$$c_1^e = \begin{cases} \tau_{0,1}^e \left(1 - \frac{\zeta^e}{\zeta^+}\right), & \text{if } 0 \leq \zeta^e \leq \zeta^+; \\ 0, & \text{if } \zeta^e > \zeta^+; \end{cases} \quad (4)$$

$$c_2^e = \begin{cases} \tau_{0,2}^e \left(1 - \frac{\zeta^e}{\zeta^+}\right), & \text{if } 0 \leq \zeta^e \leq \zeta^+; \\ 0, & \text{if } \zeta^e > \zeta^+; \end{cases} \quad (5)$$

$$b^e = \begin{cases} \sigma_0^e \left(1 - \frac{\zeta^e}{\zeta^+}\right), & \text{if } 0 \leq \zeta^e \leq \zeta^+; \\ 0, & \text{if } \zeta^e > \zeta^+, \end{cases} \quad (6)$$

τ_1^e and τ_2^e are the shear stresses in any two tangential-slip directions, σ^e is the stress normal to the surface of the microfracture, $\zeta^e = (\zeta_{t1}^{e2} + \zeta_{t2}^{e2} + \zeta_n^{e2})^{1/2}$ is the Euclidean norm of interface separation, ζ_{t1}^e and ζ_{t2}^e are the two tangential slips on the interface, and ζ_n^e is the normal separation on the interface. Initially, at the point of initiation of microfracture, c_1^e and c_2^e take on the values of the shear stresses $\tau_{0,1}^e$ and $\tau_{0,2}^e$, respectively, and b^e assumes the value of the normal stress σ_0^e .

It is necessary to write the weakening evolutions in incremental form for purposes of implementation into the AES framework. To do this, we impose the discrete consistency conditions at time t_{n+1} as follows:

$$\begin{aligned} 0 &= f_{t1,n+1}^e, \\ &= |\tau_{1,n+1}^e| - c_{1,n+1}^e, \\ &= |(\mathbf{n} \otimes \mathbf{m}_1)^s : \boldsymbol{\sigma}_{n+1}^e| - c_{1,n+1}^e, \end{aligned} \quad (7)$$

$$\begin{aligned} 0 &= f_{t2,n+1}^e, \\ &= |\tau_{2,n+1}^e| - c_{2,n+1}^e, \\ &= |(\mathbf{n} \otimes \mathbf{m}_2)^s : \boldsymbol{\sigma}_{n+1}^e| - c_{2,n+1}^e, \end{aligned} \quad (8)$$

and

$$\begin{aligned} 0 &= f_{n,n+1}^e, \\ &= \sigma_{n+1}^e - b_{n+1}^e, \\ &= (\mathbf{n} \otimes \mathbf{n}) : \boldsymbol{\sigma}_{n+1}^e - b_{n+1}^e, \end{aligned} \quad (9)$$

where

$$c_{1,n+1}^e = \begin{cases} \tau_{0,1}^e \left(1 - \frac{\zeta_{n+1}^e}{\zeta^+}\right), & \text{if } 0 \leq \zeta_{n+1}^e \leq \zeta^+; \\ 0, & \text{if } \zeta_{n+1}^e > \zeta^+; \end{cases} \quad (10)$$

$$c_{2,n+1}^e = \begin{cases} \tau_{0,2}^e \left(1 - \frac{\zeta_{n+1}^e}{\zeta^+}\right), & \text{if } 0 \leq \zeta_{n+1}^e \leq \zeta^+; \\ 0, & \text{if } \zeta_{n+1}^e > \zeta^+; \end{cases} \quad (11)$$

$$b_{n+1}^e = \begin{cases} \sigma_0^e \left(1 - \frac{\zeta_{n+1}^e}{\zeta^+}\right), & \text{if } 0 \leq \zeta_{n+1}^e \leq \zeta^+; \\ 0, & \text{if } \zeta_{n+1}^e > \zeta^+, \end{cases} \quad (12)$$

and

$$\begin{aligned} \sigma_{n+1}^e = \sigma_n^e + c^e : \frac{1}{V^e} \int_{V^e} & \left[\Delta \epsilon_{c,n+1} - \Delta \zeta_{t1,n+1}^e \left(\nabla f^h \otimes \mathbf{m}_1 \right)^s \right. \\ & \left. - \Delta \zeta_{t2,n+1}^e \left(\nabla f^h \otimes \mathbf{m}_2 \right)^s - \Delta \zeta_{n,n+1}^e \left(\nabla f^h \otimes \mathbf{n} \right)^s \right] dV \end{aligned} \quad (13)$$

and where c^e is the rank-four elastic moduli tensor, f^h is a smooth blending function that has the value of zero at the nodes on one side of the discontinuity and one at the nodes on the other side of the microfracture (see Chapter 7 of [31] for details on this blending function), and subscript ‘ $n + 1$ ’ pertains to time t_{n+1} .

The conforming displacement field can be approximated using standard finite element interpolations,

$$\mathbf{u}_c^e(\mathbf{x}) = \sum_{I \in N_{\text{nodes}}} N_{e,I}(\mathbf{x}) \mathbf{d}_I^e = \mathbf{N}_e \mathbf{d}^e, \quad (14)$$

where N_{nodes} is the number of nodes in the element, \mathbf{d}_I^e is the displacement vector at node I , and N_I^e is the shape function at node I . The finite element interpolation for the conforming strain field can be written as

$$\epsilon_c^e = \nabla^s \mathbf{u}_c^e(\mathbf{x}) = \mathbf{B}_e \mathbf{d}^e, \quad (15)$$

where \mathbf{B}_e is the element of strain–displacement matrix. We can now write the finite element equation in residual form as

$$\mathbf{r}^e = \int_{V^e} \mathbf{B}_e^T \sigma^e dV - \int_{V^e} \mathbf{N}_e^T \mathbf{f}^e dV - \int_{A^e} \mathbf{N}_e^T \hat{\mathbf{t}} dA, \quad (16)$$

along with the constraints $f_{t1}^e = f_{t2}^e = f_n^e = 0$, where V^e is the element domain and A^e is the element boundary.

Taking the variations gives

$$\delta \mathbf{r}^e = \mathbf{K}_{dd}^e \delta \mathbf{d}^e + \mathbf{K}_{d\zeta_{t1}}^e \delta \zeta_{t1}^e + \mathbf{K}_{d\zeta_{t2}}^e \delta \zeta_{t2}^e + \mathbf{K}_{d\zeta_n}^e \delta \zeta_n^e, \quad (17)$$

$$\delta f_{t1}^e = \mathbf{K}_{\zeta_{t1}d}^e \delta \mathbf{d}^e + \mathbf{K}_{\zeta_{t1}\zeta_{t1}}^e \delta \zeta_{t1}^e + \mathbf{K}_{\zeta_{t1}\zeta_{t2}}^e \delta \zeta_{t2}^e + \mathbf{K}_{\zeta_{t1}\zeta_n}^e \delta \zeta_n^e, \quad (18)$$

$$\delta f_{t2}^e = \mathbf{K}_{\zeta_{t2}d}^e \delta \mathbf{d}^e + \mathbf{K}_{\zeta_{t2}\zeta_{t1}}^e \delta \zeta_{t1}^e + \mathbf{K}_{\zeta_{t2}\zeta_{t2}}^e \delta \zeta_{t2}^e + \mathbf{K}_{\zeta_{t2}\zeta_n}^e \delta \zeta_n^e, \quad (19)$$

$$\delta f_n^e = \mathbf{K}_{\zeta_n d}^e \delta \mathbf{d}^e + \mathbf{K}_{\zeta_n \zeta_{t1}}^e \delta \zeta_{t1}^e + \mathbf{K}_{\zeta_n \zeta_{t2}}^e \delta \zeta_{t2}^e + \mathbf{K}_{\zeta_n \zeta_n}^e \delta \zeta_n^e. \quad (20)$$

Formulation of all the stiffness terms can be found in the Appendix.

For the case where the microfracture interfaces are in contact slip mode, the direction of slip is determined by the crystal structure. Thus, there is only one tangential-slip degree of freedom (DOF) for every microfractured element, and the interface yield function takes the form

$$f_t^e = \begin{cases} |\tau^e| + \mu^e \sigma^e \left(\frac{\zeta_t^e}{\zeta_t^+} \right) - c^e \left(1 - \frac{\zeta_t^e}{\zeta_t^+} \right) = 0, & \text{if } 0 \leq |\zeta_t^e| \leq \zeta_t^+; \\ |\tau^e| + \mu^e \sigma^e = 0, & \text{if } |\zeta_t^e| > \zeta_t^+, \end{cases} \quad (21)$$

where μ^e is the interface coefficient of friction and ζ_t^e is the slip magnitude in the direction of the relevant crystal slip structure.

We can write the incremental tangential consistency condition as

$$\begin{aligned} 0 &= f_{t,n+1}^e, \\ &= |\tau_{n+1}^e| + \mu_{n+1}^e \sigma_{n+1}^e - c_{n+1}^e, \\ &= |(\mathbf{n} \otimes \mathbf{m})^s + \mu_{n+1}^e (\mathbf{n} \otimes \mathbf{n})| : \boldsymbol{\sigma}_{n+1}^e - c_{n+1}^e, \end{aligned} \quad (22)$$

where

$$c_{n+1}^e = \begin{cases} \tau_0^e \left(1 - \frac{|\zeta_{t,n+1}^e|}{\zeta_t^+} \right), & \text{if } 0 \leq |\zeta_{t,n+1}^e| \leq \zeta_t^+; \\ 0, & \text{if } |\zeta_{t,n+1}^e| > \zeta_t^+; \end{cases} \quad (23)$$

$$\mu_{n+1}^e = \begin{cases} \mu \left(\frac{|\zeta_{t,n+1}^e|}{\zeta_t^+} \right), & \text{if } 0 \leq |\zeta_{t,n+1}^e| \leq \zeta_t^+; \\ 0, & \text{if } |\zeta_{t,n+1}^e| > \zeta_t^+, \end{cases} \quad (24)$$

and

$$\boldsymbol{\sigma}_{n+1}^e = \boldsymbol{\sigma}_n^e + \mathbf{c}^e : \frac{1}{V^e} \int_{V^e} \left[\Delta \epsilon_{c,n+1} - \Delta \zeta_{t,n+1}^e (\nabla f^h \otimes \mathbf{m})^s \right] dV. \quad (25)$$

The finite element equations for an element can then be written in residual form as

$$\mathbf{r}^e = \int_{V^e} \mathbf{B}_e^T \boldsymbol{\sigma}^e dV - \int_{V^e} \mathbf{N}_e^T \mathbf{f}^e dV - \int_{A^e} \mathbf{N}_e^T \hat{\mathbf{t}} dA, \quad (26)$$

subject to the constraint $f_t^e = 0$, where V^e is the element domain and A^e is the element boundary. For dead loading, the first variations take the form

$$\delta \mathbf{r}^e = \mathbf{K}_{dd}^e \delta \mathbf{d}^e + \mathbf{K}_{d\zeta_t}^e \delta \zeta_t^e, \quad (27)$$

$$\delta f_t^e = \mathbf{K}_{\zeta_t d}^e \delta \mathbf{d}^e + \mathbf{K}_{\zeta_t \zeta_t}^e \delta \zeta_t^e. \quad (28)$$

Formulation of all the stiffness terms can be found in the Appendix.

2.2. Computational homogenization

The REV of a porous rock lives in the continuum scale and reflects the rock's microstructure as well as the pore-scale mechanisms described previously. Whereas the pore-scale responses can be obtained from the finite element solution, additional computation is required to obtain the homogenized response of the REV. We now describe the homogenization procedure in the succeeding text.

Under an imposed overall homogeneous incremental strain $\delta \bar{\boldsymbol{\epsilon}}$ on the REV, the grains will deform, and microcracks will form between and through the grains. This alters the overall tangential stiffness matrix $\bar{\mathbf{K}}$ of the system, which is defined from the incremental finite element equation

$$\delta \mathbf{f} = \bar{\mathbf{K}} \delta \mathbf{d}, \quad (29)$$

where $\delta \mathbf{d}$ and $\delta \mathbf{f}$ are the incremental nodal displacement and nodal force vectors, respectively.

The incremental matrix equation can be partitioned into an interior domain and a boundary domain, that is,

$$\begin{Bmatrix} \delta f_a \\ \delta f_b \end{Bmatrix} = \begin{bmatrix} \bar{K}_{aa} & \bar{K}_{ab} \\ \bar{K}_{ba} & \bar{K}_{bb} \end{bmatrix} \begin{Bmatrix} \delta d_a \\ \delta d_b \end{Bmatrix}, \quad (30)$$

where subscripts a and b pertain to interior and exterior DOFs, respectively. Upon partitioning, static condensation [66] can be performed to express the incremental equation in terms of the boundary terms only. This results in the tangential relation

$$\delta \tilde{f} = \tilde{K} \delta \tilde{d}, \quad (31)$$

where

$$\delta \tilde{f} = \delta f_b - \bar{K}_{ba} \bar{K}_{aa}^{-1} \delta f_a, \quad (32)$$

$$\tilde{K} = \bar{K}_{bb} - \bar{K}_{ba} \bar{K}_{aa}^{-1} \bar{K}_{ab}, \quad (33)$$

$$\delta \tilde{d} = \delta d_b, \quad (34)$$

$$\delta d_a = \bar{K}_{aa}^{-1} (\delta f_a - \bar{K}_{ab} \delta d_b). \quad (35)$$

The homogenized tangent constitutive tensor for the REV can be calculated from the matrix equation

$$\mathcal{C} = N_\sigma \tilde{K} N_\epsilon, \quad (36)$$

where N_σ and N_ϵ are homogenization operators defined such that

$$\delta \tilde{d} = N_\epsilon \delta \bar{\epsilon}, \quad \delta \bar{\sigma} = N_\sigma \delta \tilde{f}. \quad (37)$$

Note that a singular \tilde{K} does not necessarily imply a singular \mathcal{C} because the matrix \tilde{K} is typically much larger in dimension than the matrix \mathcal{C} . Physically, this could imply that grains could chip off locally from the solid matrix resulting in disconnected nodes and a singular \tilde{K} , but unless the entire solid matrix collapses, \mathcal{C} remains non-singular. Evidently, the operators N_σ and N_ϵ influence the bifurcation of the REV into a deformation band mode.

The operator N_ϵ relates the incremental displacement at the boundary with the overall homogeneous deformation. Consider a microstructure embedded in a unit cell. Assume that the unit cell is subjected to a homogeneous velocity gradient $\nabla \bar{v}$. The homogeneous velocity field in the unit cell, ignoring rigid body modes, is then given by the equation

$$\bar{v} = (\nabla \bar{v}) \cdot \mathbf{x}. \quad (38)$$

Now, consider the microstructure to be discretized into finite elements with n_{nodes} = number of nodes and $n_{\text{dof}} = n_{\text{sd}} \times n_{\text{nodes}}$ = total number of DOFs (with n_{sd} = number of spatial dimensions, equal to 2 or 3). The total number of boundary nodes is denoted by n_{bd} .

We can assemble $\delta \tilde{d}$ from the individual-boundary nodal vectors consisting of $\{\delta \tilde{d}_1, \dots, \delta \tilde{d}_{n_{\text{bd}}}\}$, where

$$\frac{\delta \tilde{d}_A}{\delta t} = (\nabla \bar{v}) \cdot \mathbf{x}_A = \mathbf{H}_A \{\nabla \bar{v}\}, \quad (39)$$

$\{\nabla \bar{v}\}$ is the same as the tensor $\nabla \bar{v}$ but in vector form, and \mathbf{H}_A is a rectangular matrix with nodal coordinates \mathbf{x}_A as elements, that is,

$$\mathbf{H}_A = \begin{bmatrix} x_{1A} & 0 & 0 & \frac{1}{2}x_{2A} & 0 & \frac{1}{2}x_{3A} \\ 0 & x_{2A} & 0 & \frac{1}{2}x_{1A} & \frac{1}{2}x_{3A} & 0 \\ 0 & 0 & x_{3A} & 0 & \frac{1}{2}x_{2A} & \frac{1}{2}x_{1A} \end{bmatrix}, \quad (40)$$

where x_{iA} is the coordinate of the i th DOF of nodal point A . This gives

$$\dot{\mathbf{d}} := \frac{\delta \tilde{\mathbf{d}}}{\delta t} = \mathbf{H} \{ \nabla \bar{\mathbf{v}} \}, \quad \mathbf{H} = \begin{bmatrix} \mathbf{H}_1 \\ \vdots \\ \mathbf{H}_N \end{bmatrix}. \quad (41)$$

Therefore, we obtain

$$\dot{\mathbf{d}} = \mathbf{H} \{ \nabla \bar{\mathbf{v}} \} = \mathbf{H} \dot{\bar{\boldsymbol{\epsilon}}} = \mathbf{N}_\epsilon \dot{\bar{\boldsymbol{\epsilon}}}, \quad (42)$$

where $\dot{\bar{\boldsymbol{\epsilon}}} := \delta \bar{\boldsymbol{\epsilon}} / \delta t$.

The homogenization operator \mathbf{N}_σ can be obtained by averaging the nodal force vector $\delta \mathbf{f}$ using the principle of virtual work. The result takes the form

$$\begin{aligned} \delta \bar{\boldsymbol{\sigma}} &= \frac{1}{V} \sum_{A=1}^{n_{\text{bd}}} \delta \tilde{\mathbf{f}}_A \cdot \mathbf{x}_A \\ &= \frac{1}{V} [\mathbf{H}_1^T \cdots \mathbf{H}_{n_{\text{bd}}}^T] \left\{ \begin{array}{c} \delta \tilde{\mathbf{f}}_1 \\ \vdots \\ \delta \tilde{\mathbf{f}}_{n_{\text{bd}}} \end{array} \right\} \\ &= \frac{1}{V} \mathbf{H}^T \delta \tilde{\mathbf{f}} \equiv \mathbf{N}_\sigma \delta \tilde{\mathbf{f}} \end{aligned} \quad (43)$$

The homogenization procedure outlined previously is similar in principle to that proposed by Miehe and Koch [49] for affine deformation on the REV boundaries. The challenge in the present work lies explicitly in dealing with voids and microfractures to obtain the homogenized response. A byproduct of the homogenization is the overall constitutive tangent operator for the REV. However, this operator contains multiple branches depending on the loading direction. Each possible loading direction triggers different sets of microfractures and thus must be probed to determine the most critical mode of shear band bifurcation.

2.3. Incremental nonlinearity and bifurcation

Throughout this work, we use the classic condition for shear band bifurcation proposed by Rudnicki and Rice [3]. Although closed-form analytical solutions for bifurcation are available for some simple plasticity models [67], they are not so useful for most problems particularly in the present case where incremental nonlinearity is involved. A preferred approach would be to determine the critical mode numerically. To this end, the notion of localization function would be useful [2, 31]. The localization function \mathcal{F} is the determinant of the so-called acoustic tensor \mathcal{A} , which is evaluated from the tangent constitutive tensor \mathcal{C} and attains a minimum value for some shear band orientation \mathbf{n} , that is,

$$\mathcal{F} = \min_{|\mathbf{n}|} \det(\mathcal{A}), \quad \mathcal{A} = \mathbf{n} \cdot \mathcal{C} \cdot \mathbf{n}, \quad (44)$$

A numerical search for this critical orientation is part of the computational problem [68–71]; the other part is the determination of the critical homogenized constitutive tangent operator \mathcal{C} that varies with loading direction because of the incremental nonlinearity of the constitutive response. Each of these aspects is elaborated in the following discussion.

Continuum bifurcation on the scale of the REV is primarily caused by slip weakening processes after microfracture formation. Slip weakening, in turn, is a combination of cohesion softening and friction hardening [31], and for 3D bifurcation, gives rise to a total of nine stiffness terms [30]. One of the stiffness terms, $\mathbf{K}_{\zeta_{t1}\zeta_{t1}}^e$, has the form

$$\begin{aligned} \mathbf{K}_{\zeta_{t1}\zeta_{t1}}^e &= \left. \frac{\partial f_{t1}^e}{\partial \zeta_{t1}^e} \right|_{n+1}, \\ &= \text{sign}(\tau_1^e) (\mathbf{n} \otimes \mathbf{m}_1)^s : \left. \frac{\partial \boldsymbol{\sigma}^e}{\partial \zeta_{t1}^e} \right|_{n+1} - \left. \frac{\partial c_1^e}{\partial \zeta_{t1}^e} \right|_{n+1}, \end{aligned} \quad (45)$$

where (removing the sign ‘ $|_{n+1}$ ’ from now on for brevity)

$$\begin{aligned}\frac{\partial c_1^e}{\partial \zeta_{t1}^e} &= \frac{\partial}{\partial \zeta_{t1}^e} \left[\tau_{0,1}^e \left(1 - \frac{\zeta^e}{\zeta^+} \right) \right], \\ &= \frac{\partial}{\partial \zeta_{t1}^e} \left[\tau_{0,1}^e \left(1 - \frac{1}{\zeta^+} \sqrt{\zeta_{t1}^{e2} + \zeta_{t2}^{e2} + \zeta_n^{e2}} \right) \right], \\ &= -\tau_{0,1}^e \frac{\zeta_{t1}^e}{\zeta^+ \zeta^e}.\end{aligned}\quad (46)$$

Similarly, $\mathbf{K}_{\zeta_{t1}\zeta_{t2}}^e$ and $\mathbf{K}_{\zeta_{t1}\zeta_n}^e$ can be evaluated as

$$\begin{aligned}\mathbf{K}_{\zeta_{t1}\zeta_{t2}}^e &= \frac{\partial f_{t1}^e}{\partial \zeta_{t2}^e}, \\ &= \text{sign}(\tau_1^e) (\mathbf{n} \otimes \mathbf{m}_1)^s : \frac{\partial \boldsymbol{\sigma}^e}{\partial \zeta_{t2}^e} - \frac{\partial c_1^e}{\partial \zeta_{t2}^e}, \\ &= \text{sign}(\tau_1^e) (\mathbf{n} \otimes \mathbf{m}_1)^s : \frac{\partial \boldsymbol{\sigma}^e}{\partial \zeta_{t2}^e} + \tau_{0,1}^e \frac{\zeta_{t2}^e}{\zeta^+ \zeta^e},\end{aligned}\quad (47)$$

$$\begin{aligned}\mathbf{K}_{\zeta_{t1}\zeta_n}^e &= \frac{\partial f_{t1}^e}{\partial \zeta_n^e}, \\ &= \text{sign}(\tau_1^e) (\mathbf{n} \otimes \mathbf{m}_1)^s : \frac{\partial \boldsymbol{\sigma}^e}{\partial \zeta_n^e} - \frac{\partial c_1^e}{\partial \zeta_n^e}, \\ &= \text{sign}(\tau_1^e) (\mathbf{n} \otimes \mathbf{m}_1)^s : \frac{\partial \boldsymbol{\sigma}^e}{\partial \zeta_n^e} + \tau_{0,1}^e \frac{\zeta_n^e}{\zeta^+ \zeta^e},\end{aligned}\quad (48)$$

Note that these terms arise when the sliding distance ζ^+ has not been exceeded. Once the sliding distance is reached, the second term in each of the stiffness terms that signifies cohesion softening will go to zero. Formulation of the other six stiffness terms can be found in the Appendix.

To accommodate the incremental nonlinearity of the constitutive response, it is necessary to conduct a series of strain probes covering all six directions of the strain tensor. We can, however, represent a plot only in three dimensions. The probe directions are defined as follows to accommodate visualization:

$$\begin{Bmatrix} \Delta \epsilon_{xx} \\ \Delta \epsilon_{yy} \\ \Delta \epsilon_{zz} \end{Bmatrix} = \Delta \epsilon_{\text{probe}} \begin{Bmatrix} \cos(\theta) \cos(\phi) \\ \sin(\phi) \\ \sin(\theta) \cos(\phi) \end{Bmatrix}\quad (49)$$

for the normal strains, and

$$\begin{Bmatrix} \Delta \epsilon_{xy} \\ \Delta \epsilon_{yz} \\ \Delta \epsilon_{xz} \end{Bmatrix} = \Delta \epsilon_{\text{probe}} \begin{Bmatrix} \cos(\alpha) \cos(\psi) \\ \sin(\psi) \\ \sin(\alpha) \cos(\psi) \end{Bmatrix}\quad (50)$$

for the shear strains, where θ , ϕ , α , and ψ are the Euler angles and $\Delta \epsilon_{\text{probe}}$ is the magnitude of the strain probe. The angles ϕ and ψ vary from 0 to 2π with increments of 0.286, while θ and α vary from 0 to π with the same increments. It is understood that the two 3D plots do not exhaust all the possible probe directions in six dimensions. Such investigation has been conducted despite not being reported. The strain probes can be plotted as shown in Figure 1, where the three axes of Cartesian coordinates represent the three principal strain components $\Delta \epsilon_{xx}$, $\Delta \epsilon_{yy}$, and $\Delta \epsilon_{zz}$ (in the figure, $\Delta \epsilon_{\text{probe}} = 1.0$, but this is not always the case). A similar plot can be produced with $\Delta \epsilon_{xy}$, $\Delta \epsilon_{yz}$, and $\Delta \epsilon_{xz}$ as the axes of Cartesian coordinates. Euler angles relating the strain probe direction and the fixed reference frame for the normal strains are shown in Figure 2. The coordinates are obtained by a positive (right-hand rule) rotation of θ about the y -axis followed by a positive rotation of ϕ about the z_c -axis.

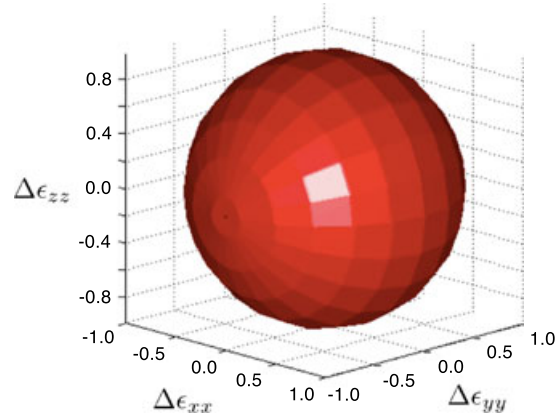


Figure 1. Normal strain probes in three-dimensional Cartesian coordinate system. Full strain probes require representation in six-dimensional space.

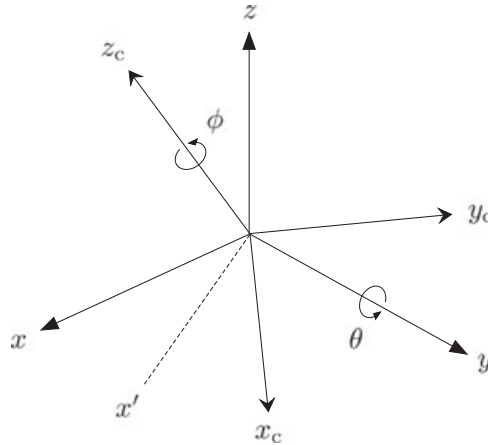


Figure 2. Euler angles describing the relationship between the crystal reference frame and the fixed reference frame.

The stress response envelope produced from the strain probes can be obtained and then plotted in three dimensions.

The magnitude of the strain probe $\Delta\epsilon_{\text{probe}}$ should be small enough because the response to the strain loading is nonlinear. Kishino [40] used a magnitude of stress probes that was one-hundredth of the initial confining pressure. For Royis and Doanh [36] and Calvetti *et al.* [32], this number was one-tenth of the initial confining pressure.

From the strain probes, the stress response envelope can be obtained. In this paper, the stress response is reported in terms of the incremental von Mises stress for each of the strain probes. The von Mises stress q can be calculated from the stress tensor σ in three dimensions as

$$q = \sqrt{\frac{(\sigma_{xx} - \sigma_{yy})^2 + (\sigma_{yy} - \sigma_{zz})^2 + (\sigma_{zz} - \sigma_{xx})^2 + 6(\sigma_{xy}^2 + \sigma_{yz}^2 + \sigma_{zx}^2)}{2}}. \quad (51)$$

The incremental von Mises stress is the difference $\Delta q = q_{n+\epsilon} - q_n$, where $q_{n+\epsilon}$ is the value at the end of a strain probe and q_n is the value at the beginning of the probe (which corresponds to the current ‘converged’ stress configuration). To report the stress response for the series of strain probes in three dimensions, a plot similar to Figure 1 is generated, with the magnitude representing Δq .

Apart from the stress response envelope, it is also possible to obtain the plastic strain response envelope. The incremental homogenized plastic strain can be obtained from the equation

$$\Delta \boldsymbol{\epsilon}^P = \Delta \boldsymbol{\epsilon} - \Delta \boldsymbol{\epsilon}^e = \Delta \boldsymbol{\epsilon} - \mathbf{D}^{e-1} \Delta \boldsymbol{\sigma}, \quad (52)$$

where $\Delta \boldsymbol{\sigma}$ and $\Delta \boldsymbol{\epsilon}$ represent the incremental homogenized stress and strain, respectively, in Voigt notation, that is,

$$\Delta \boldsymbol{\sigma} = \begin{Bmatrix} \Delta \sigma_{xx} \\ \Delta \sigma_{yy} \\ \Delta \sigma_{zz} \\ \Delta \sigma_{xy} \\ \Delta \sigma_{yz} \\ \Delta \sigma_{xz} \end{Bmatrix}, \quad \Delta \boldsymbol{\epsilon} = \begin{Bmatrix} \Delta \epsilon_{xx} \\ \Delta \epsilon_{yy} \\ \Delta \epsilon_{zz} \\ 2\Delta \epsilon_{xy} \\ 2\Delta \epsilon_{yz} \\ 2\Delta \epsilon_{xz} \end{Bmatrix}, \quad (53)$$

where \mathbf{D}^e is the homogenized second-order elastic tangent constitutive tensor, which is also written in Voigt notation, and $\Delta \boldsymbol{\epsilon}^e$ and $\Delta \boldsymbol{\epsilon}^P$ are the elastic and plastic components of the incremental homogenized strain, respectively. This technique of obtaining the plastic strain is similar to that used by Calvetti *et al.* [32], whereas Kishino [40] employed a closed stress path in which incremental loading and unloading were performed to obtain the residual strain that became the plastic component of the incremental strain. The homogenized elastic tangent constitutive tensor \mathbf{D}^e consists of the elastic stiffnesses of all the elements within the REV and is constant for every time step and every strain probe. The constitutive matrix \mathbf{D}^e may be obtained from the homogenized response at the end of the very first time step, which is always elastic in all our simulations.

3. NUMERICAL EXAMPLES

In the following examples, we investigate the behavior of a crystalline rock with mechanical properties similar to those of limestone. The homogenized response is obtained from pore-scale mechanisms involving microfracturing, with fracture plane and slip direction informed by the crystallographic structure of the rock. The algorithm is such that once the crystal yield stress is reached on the primary slip plane, localization takes place and the slip plane becomes the site of microfracture formation and initiation. Table I shows the mechanical properties of the rock. The crystal yield stress, τ_Y , is assumed to be the same for all the crystallographic slip planes.

A cubic REV is used to model the microstructure. The REV is a $20 \times 20 \times 20 \mu\text{m}^3$ cube divided into $8 \times 8 \times 8$ cubical elements. Some of the elements are void elements so that the porosity of the REV is 9.38% as shown in Figure 3. The voids feature sharp corners and edges that attract local stress concentration, in agreement with the experimental observations of Mowar *et al.* [29] that microfractures generally initiate on the peripheries of voids because of irregular pore geometry. In addition, the solid component of the REV are crystals with different orientations. The relationship of the crystal reference frame with respect to the fixed reference frame is defined by the Euler angles shown in Figure 2. Two different crystal groups within the REV is shown in Figure 3 where crystal group with Orientation #1 is shown shaded in gray while Orientation #2 is shown shaded in orange. The crystal groups possess distinct crystal orientations as reflected in Table II.

Limestone is predominantly made up of calcite, dolomite, and aragonite and thus has a complex crystal lattice. As a simplifying assumption, the crystal lattice in our model is assumed to be made up of face-centered cubic (f.c.c) crystals. An f.c.c. crystal has eight $\{1\ 1\ 1\}$ octahedral planes, each

Table I. Material properties for crystalline rock similar to limestone.

Parameter	Symbol	Value
Young's modulus	E	20,000 MPa
Poisson's ratio	ν	0.30
Crystal yield stress	τ_Y	30 MPa

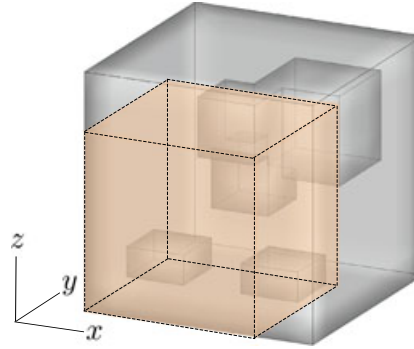


Figure 3. Partition of representative elementary volume into solid material and air voids, as well as into crystal groups with Orientation #1 (shaded gray) and Orientation #2 (shaded orange).

Table II. Euler angles of the crystal groups in degrees.

Orientation	θ	ϕ
#1	0.0	22.0
#2	0.0	0.0

with three $\langle 110 \rangle$ slip directions, resulting in 24 potentially active slip systems. In our simulation, the first slip system to activate becomes the primary system on which microfracture forms. The REV is deformed at every time step, and strain probes are applied thereafter to investigate the incremental response at the end of each time step. As such, the homogenized responses of the REV in the form of incremental plastic strain, incremental stress, or minimum determinant for shear band bifurcation can be obtained at the end of all the time steps and at the end of all the strain probes after each time step, each shedding light onto different aspects of the mechanical behavior of the porous material.

3.1. Combined shearing and extension

Under this loading condition, the six faces of the REV experience affine deformation that generates shearing and extension within the volume. At every time step, the displacements on the REV boundaries are incremented linearly. Each incremental displacement (in nanometers) takes the form

$$\begin{Bmatrix} \Delta u_x \\ \Delta u_y \\ \Delta u_z \end{Bmatrix} = 0.0125 \begin{Bmatrix} (x + 10) + (z + 10) \\ 0 \\ (x + 10) + (z + 10) \end{Bmatrix} \text{ nm}, \quad (54)$$

where x , y , z are Cartesian coordinates in microns. With boundary displacement in the y -direction being restrained, this loading condition creates a plane strain condition on the xz -plane, as shown in Figure 4(a).

The characteristic distance ζ^+ is both a physically meaningful quantity and a regularization parameter that controls the rate of softening as the microfracture develops. However, it is not a material property. For specimen-size Westerly granite, Wong [72] estimated this distance to be on the order 0.5 mm. Clearly, this distance is too large for nanometer and micron-size fractures and too small for kilometer-scale processes such as geologic faulting during dynamic earth rupture [73, 74]. Therefore, ζ^+ must be scaled to make the resulting model response meaningful. For most of the simulations, ζ^+ is assumed to have the value $2.5 \times 10^{-3} \mu\text{m}$. Parametric studies will later confirm an expected trend that the timing of continuum bifurcation depends on this parameter in the sense that smaller values of ζ^+ lead to earlier shear band bifurcation.

To gain some insight into the nature of pore-scale deformation resulting from this imposed overall deformation, Figures 5 and 6 show the evolution of the normal separation and tangential slip

within the REV for heterogeneous and homogeneous crystal orientations, respectively [30]. Crystal orientations for the heterogeneous simulation are depicted as Orientations #1 and #2 in Table II, whereas those for the homogeneous simulation are given by Orientation #2 for both crystal groups. It is evident from these two figures that crystal orientations do impact the resulting normal separation and tangential slip at the pore scale. Note that the simulations presented in [30] utilized slightly different pore structure than the one shown in Figure 3.

Figure 7 shows the evolution of the overall von Mises stress with time. Microfractures initially develop after Time Step (TS) #31, but the first stress drop occurs at TS#48. This implies that a certain number of microfractures must develop to induce an overall softening response on the REV. This statement is confirmed by the histogram shown in Figure 8. In this figure, fracture density is the ratio

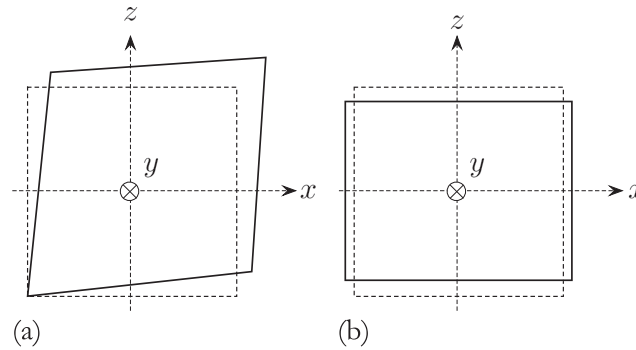


Figure 4. Affine deformation on the six faces of the representative elementary volume: (a) combined shearing and extension; (b) vertical compression and lateral extension with net volume decrease.

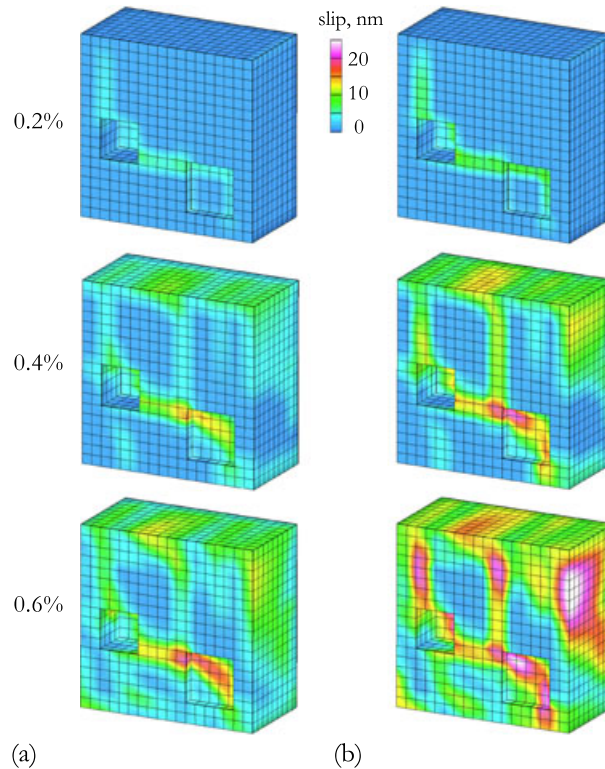


Figure 5. Evolution of: (a) normal and (b) tangential micro-slip for the combined shearing and extension simulation with heterogeneous crystal orientation. Numbers in percent are imposed volumetric strain on the representative elementary volume. After Tjioe and Borja [30].

between the total number of damaged elements and the total number of solid elements: a fracture density of zero implies that all solid elements are intact, whereas 100% means that microfractures have formed in all solid elements. Each bin represents the sum of new solid elements that developed microfractures over five time step values. Thus, the bin at TS#50 totals the number of elements that developed microfractures from TS#48 to TS#52. Initially, only one or two microfractures have formed, but this number quickly increases at bin #45, which explains the stress drop observed in Figure 7. The new microfractures are approximately evenly distributed from bin #45 to bin #105, with the peak being at bin #105 where a large overall stress drop has been observed. Thereafter, the new microfracture activity dies away as the cumulative microfracture density reaches 100%.

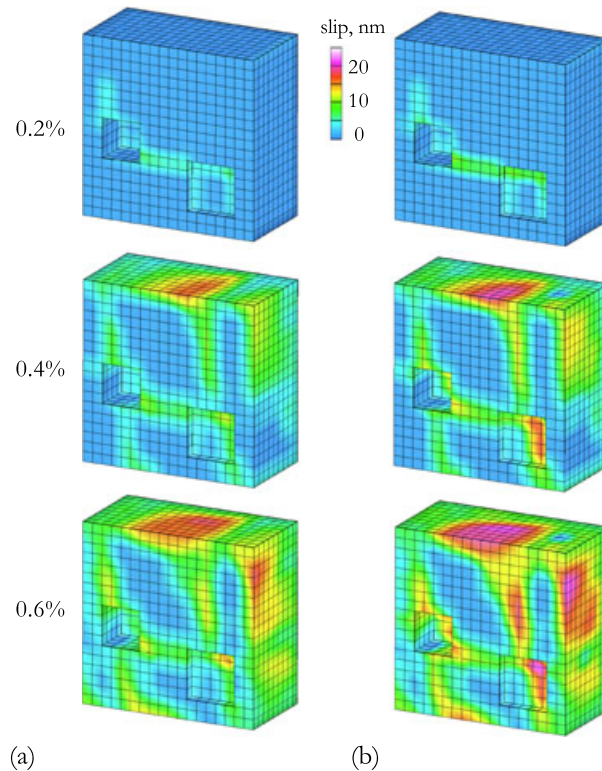


Figure 6. Evolution of: (a) normal and (b) tangential micro-slip for the combined shearing and extension simulation with homogeneous crystal orientation. Numbers in percent are imposed volumetric strain on the representative elementary volume. After Tjioe and Borja [30].

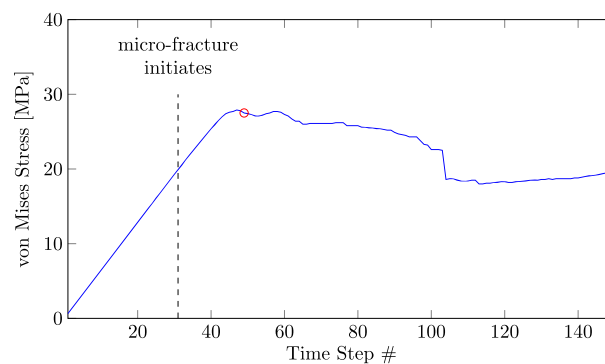


Figure 7. Variation of overall von Mises stress with time for the combined shearing and extension loading simulation. Red circle is the bifurcation point.

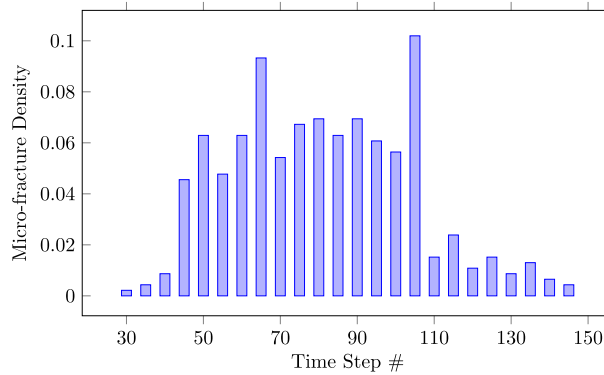


Figure 8. Histogram of microfracture density for the combined shearing and extension simulation.

Strain probes are conducted at the end of each time step with $\Delta\epsilon_{\text{probe}}$ set to $2.5e-6$. The intent of strain probing is to identify sets of microfractures triggered by certain loading directions. The magnitude of the probe must be small enough so as to capture the softening induced by slip weakening, that is, the slip on any microfracture does not exceed ζ^+ . In previous work [30], which focused mainly on deformation and not on bifurcation, typical time steps were sufficiently large that each time step induced complete slip weakening on every microfracture triggered during that time step. However, this is not the case with strain probing. The magnitude of the probe mentioned previously is sufficiently large to initiate slip weakening on the given probe direction, but is also small enough that the resulting slip does not exceed ζ^+ .

Only a few of the responses are plotted, namely, those obtained at the end of TS#48 and TS#49. Responses in the form of localization function \mathcal{F} can be visualized in Figures 9 and 10. The direction of the vector represents the strain components. To facilitate visualization, the magnitude of the vector is set to a value of 1.0 for probes that yield positive values of \mathcal{F} and a value of 1.5 for probes with negative values (these numbers are arbitrary and were chosen solely for visualization purposes). The color contour represents the natural logarithm of \mathcal{F} , except for probes with negative \mathcal{F} , which is displayed in gray color. Note that the color contour does not provide information about the magnitude of negative \mathcal{F} .

The localization function is positive for all probe directions prior to and up until TS#48, but at TS#49, a ridge was formed for certain probe directions, signaling shear band bifurcation in the REV. Microfracture formation that still leaves positive values of \mathcal{F} at TS#49 can be detected through the variation in the plot color. Observe from the contour for TS#48 that the same side of the ball (yellow) is where the ridge formed in TS#49 and that the sign of \mathcal{F} flipped from very large positive values to negative values, suggesting that the numerical value of \mathcal{F} alone does not indicate whether or not the REV is ‘stable’ in the sense of shear band bifurcation. Also note for TS#48 that the shinier side of the ball (yellow) covers a large area, indicating propensity of the REV for shear band bifurcation in many possible directions defined by that area. This is affirmed by the ridge that formed on the same side of the ball for TS#49, which also covers a large area. In principle, one can zero-in on the most critical strain probe direction by subdividing the time interval between TS#48 and TS#49 into increments (i.e., refining the time step); this is not done for this example. However, the next example shows that a narrower ridge formed for the compression–extension simulation, thus facilitating easier identification of the most critical probe direction for shear band bifurcation.

Despite the propensity of the REV to bifurcate into a shear band mode over a large expanse of strain probes shown in Figures 9 and 10, close inspection of the results reveals that there were only two different bifurcation directions across all the strain probes for TS#49 that yield negative minimum determinants. Furthermore, the two normal directions to the shear bands are nearly the same, with

$$\mathbf{n}^{(1)} = \begin{Bmatrix} 0.81 \\ -0.41 \\ 0.42 \end{Bmatrix} \quad \text{and} \quad \mathbf{n}^{(2)} = \begin{Bmatrix} 0.82 \\ -0.39 \\ 0.42 \end{Bmatrix}.$$

Because the determinant function \mathcal{F} has a negative value, the acoustic tensor \mathbf{A} is not exactly singular, and only an approximate eigenvector \mathbf{m} for this tensor can be obtained. For the present purpose, the unit eigenvector \mathbf{m} was calculated by solving two of its components in terms of the third component, yielding a normalized eigenvector equal to

$$\mathbf{m}^{(1)} \approx \mathbf{m}^{(2)} = \begin{Bmatrix} 0.63 \\ 0.41 \\ 0.65 \end{Bmatrix}.$$

The sign of \mathbf{m} has been chosen so that the vector product $\mathbf{m} \cdot \mathbf{n} > 0$ defines a dilatant shear band [1, 2].

The response envelopes of the incremental strain components can be obtained for probes at the end of every time step. However, only two such envelopes at TS#48 and TS#49 are plotted, as shown in Figures 11 and 12, respectively. For each figure, the incremental plastic and elastic strain components of the response envelope are plotted. Because probes are deformation-driven, the sum of the plastic and elastic components always give an incremental total strain of magnitude $\Delta\epsilon_{\text{probe}} = 2.5e-6$. The incremental total strain envelope is thus a sphere with radius equal to $\Delta\epsilon_{\text{probe}}$ and as

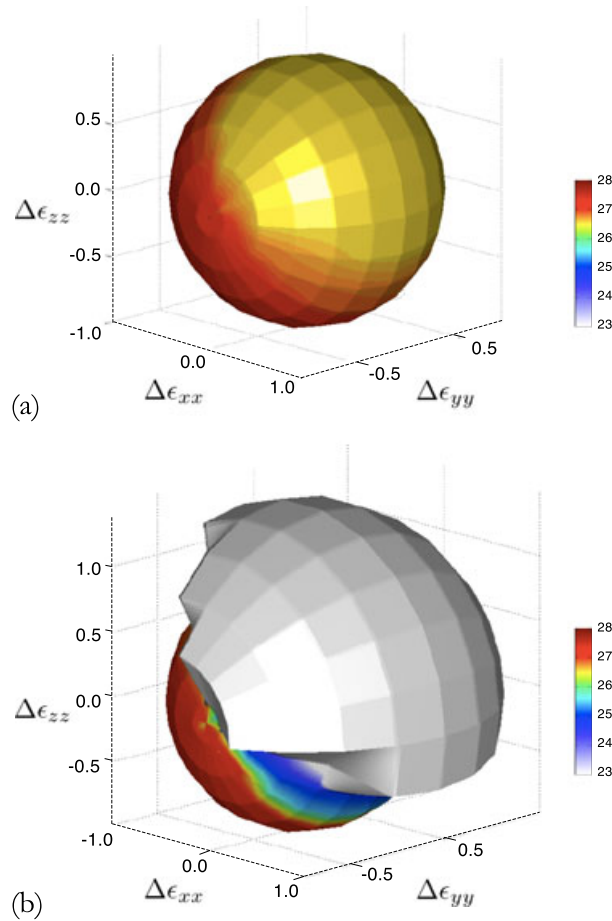


Figure 9. Localization function in the space of incremental normal strains for combined shearing and extension: (a) TS#48, (b) TS#49. Color bar is natural logarithm of \mathcal{F} . TS, Time Step.

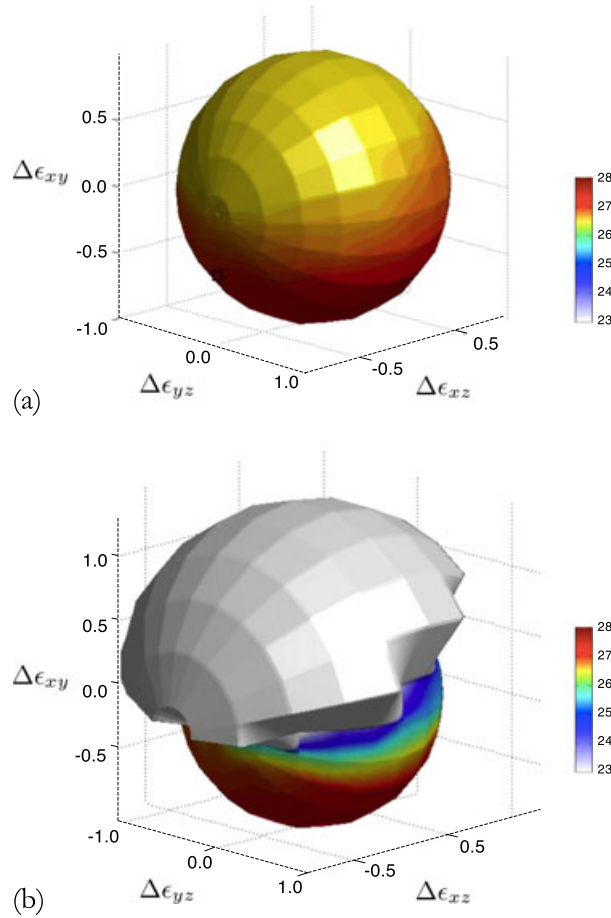


Figure 10. Localization function in the space of incremental shearing strains for combined shearing and extension: (a) TS#48, (b) TS#49. Color bar is natural logarithm of \mathcal{F} . TS, Time Step.

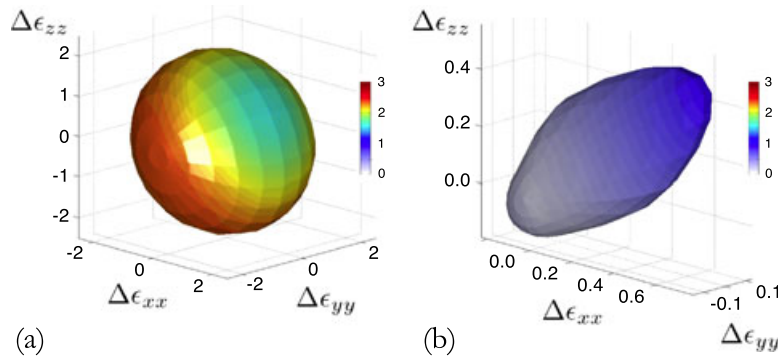


Figure 11. Strain increments for the representative elementary volume at TS#23: (a) elastic strain increment and (b) plastic strain increment. Axes and color bars are multiplied by 10^{-6} . TS, Time Step.

such, it is trivial and is not plotted along with the strain components. In both figures, the dependence of the direction of the incremental plastic strain on the strain probe direction is apparent. This implies that classic non-associative elastoplasticity relying on a single plastic flow mechanism is insufficient to describe such behavior. The incremental elastic component of strain responses plotted in Figures 11 and 12 clearly have different magnitudes for different strain probe directions. This implies that the tangent stiffness of the REV varies depending on direction of the strain probe, which is a characteristic of an incrementally nonlinear response.

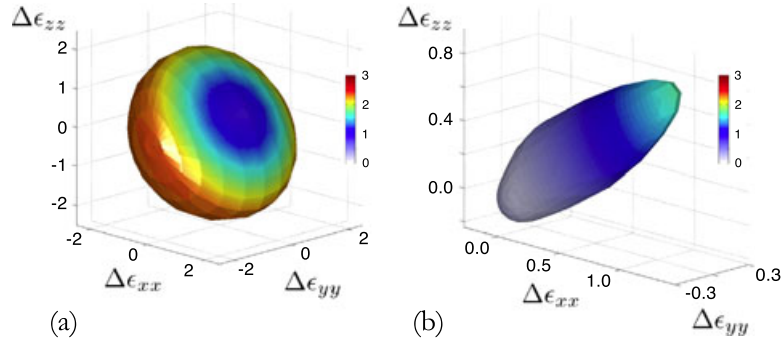


Figure 12. Strain increments for the representative elementary volume at TS#25: (a) elastic strain increment, and (b) plastic strain increment. Axes and color bars are multiplied by 10^{-6} . TS, Time Step.

Probe responses in the form of incremental von Mises stress are plotted in Figure 13. The direction of the vector from the origin to each point represents the relative proportion of the principal strain probe components $\Delta\epsilon_{xx}$, $\Delta\epsilon_{yy}$, and $\Delta\epsilon_{zz}$. The magnitude of this vector represents the incremental von Mises stress response (in megapascal) to a strain probe direction after a constant has been added to prevent the reversal of probe direction because of the introduction of negative stress values. Note that the constant varies from one time step to another. The color contour represents the true value of the incremental von Mises stress. It diverges from white color representing a zero value to two different colors representing positive and negative plot values, respectively. It can be observed from the figure that the von Mises stress increases in certain probe directions, while it decreases in other directions. Bifurcation predominantly occurs in the probe directions that yield negative values of the incremental von Mises stress.

From the simulation, it can be concluded that pore-scale mechanism in the form of microfracturing that takes into account the crystal orientations produces incrementally nonlinear behavior of the REV. Through homogenization, the constitutive tangent operator of the REV can be obtained, and bifurcation analysis can be conducted to detect points in which the REV bifurcates into a shear band. Information about the bifurcation points can subsequently be used in the larger scale simulation to signal the change in the constitutive behavior. Finally, it must be pointed out that the REV should theoretically develop a macroscale shear band at the bifurcation point, represented by the red circle in Figure 7. The kinematics of this macroscale shear band is not represented by the responses beyond the red circle shown in Figure 7, because we have continued to use the same affine boundary displacements on the faces of the REV even though we have already detected shear band bifurcation in the solution.

3.2. Combined compression and lateral extension

Under this loading condition, the REV experiences an affine deformation in which its top and bottom faces compress while the other four lateral faces stretch, as shown in Figure 4(b). The incremental displacements of the faces of the cube are given by

$$\begin{Bmatrix} \Delta u_x \\ \Delta u_y \\ \Delta u_z \end{Bmatrix} = \begin{Bmatrix} 0.0225x \\ 0.0225y \\ -0.05z \end{Bmatrix} \text{ nm}, \quad (55)$$

where x , y , and z are Cartesian coordinates in microns. The extension of the lateral faces is 45% of the vertical compression, so minimal lateral compressive stress is produced. We take $\zeta^+ = 2.5 \times 10^{-3} \mu\text{m}$ and coefficient of friction $\mu = 0.75$ on the contact faces.

A plot of the von Mises stress for the different time steps is shown in Figure 14. Microfractures initially develop in the REV at TS#37. However, the stress continues to increase at almost the same slope before a discernible stress drop occurs at TS#63. Shear band bifurcation, represented by the red circle in Figure 14, is then detected almost immediately thereafter. However, the frictional resistance on the microfracture surface continues to increase because of the increase in normal

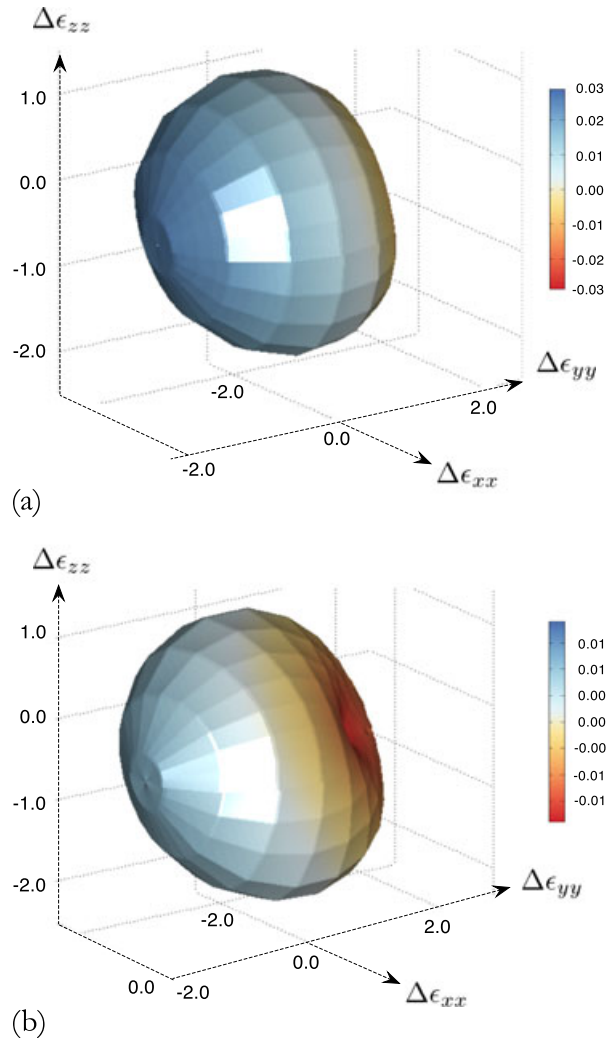


Figure 13. Incremental von Mises stress: (a) TS#48, (b) TS#49. Color bar in megapascal (MPa). TS, Time Step.

stress. Hardening occurs subsequently as the increase in friction results in shear stress buildup that eventually causes the interfaces to stop slipping.

Figure 15 depicts a histogram showing the evolution of microfracture density with time. The histogram approximately follows a normal distribution where the peak is reached at bin #60, which coincides with the timing of softening and drop in the von Mises stress. The greatest number of micro-activity is in the bins ranging from TS#45 to TS#80. The activities subside thereafter as the von Mises stress increases in a nearly linear fashion (Figure 14).

To investigate shear band bifurcation, we again apply strain probes with $\Delta\epsilon_{\text{probe}} = 2.5\text{e-}6$ and plot the variation of the localization function \mathcal{F} . Figure 16 shows a profile of this function obtained from the probes for TS#63 and TS#64. The magnitude of the vector is set to a value of 1.0 for probes that yield positive \mathcal{F} and 1.5 for probes with negative values. The color contour represents the natural logarithm of \mathcal{F} , except for probes with negative \mathcal{F} , which is displayed in gray color. A ridge of negative \mathcal{F} can be observed at TS#64, which is the first instance that it has formed, implying shear bifurcation occurring between this and the previous time steps. Note that the ridge is not as widespread as the one that formed in the previous example; nevertheless, it is still a ridge and not a spike, implying that there are still several possible critical modes of bifurcation. Variation in the plot color also shows that different sets of microfractures formed during probing, causing variations in the tangent operator.

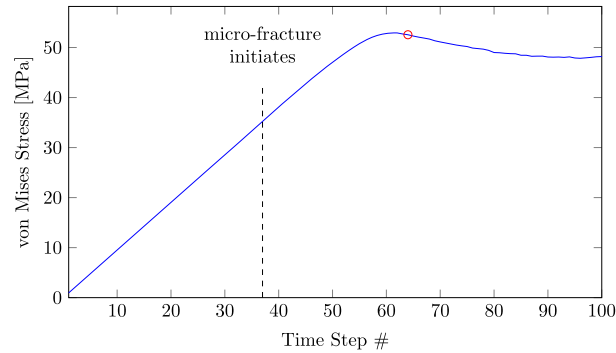


Figure 14. Variation of overall von Mises stress with time for the combined vertical compression and lateral extension loading simulation. Red circle is bifurcation point.

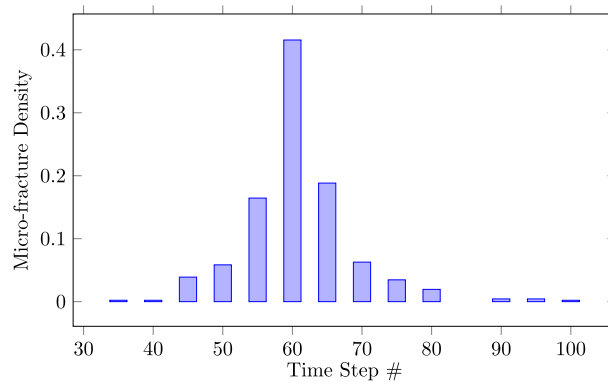


Figure 15. Histogram of microfracture density for the combined vertical compression and lateral extension simulation.

Despite the fact that the ridge is not as widespread as the one that formed in the shearing/extension simulation, a close inspection of the ensuing shear band orientations reveals that there were at least 20 shear band orientations detected that yielded the most negative minimum determinants. However, the shear band orientations were nearly the same, with the components of \mathbf{n} having values given by the range

$$\mathbf{n}^{(1,2,\dots,20)} = \begin{pmatrix} 0.38, \dots, 0.46 \\ 0.57, \dots, 0.60 \\ 0.68, \dots, 0.69 \end{pmatrix} \quad (56)$$

and eigenvectors equal to

$$\mathbf{m}^{(1)} \approx \dots \approx \mathbf{m}^{(20)} = \begin{pmatrix} -0.34 \\ -0.60 \\ 0.72 \end{pmatrix}, \quad (57)$$

where the sign of \mathbf{m} was chosen so that $\mathbf{m} \cdot \mathbf{n} < 0$ defines a compactive shear band [1, 2]. These results and those from the combined extension and shearing simulations, indicate strong dependence of shear band orientation on the stress state, but the effect of strain probes on shear band orientation appears to be in second order. Note that the vector \mathbf{m} is nearly perpendicular to the vector \mathbf{n} for this example, suggesting little volume change during bifurcation.

Figures 17 and 18 show the incremental elastic and plastic strain response envelopes for probes at the end of TS#63 and TS#64, respectively. As in the previous example, the incremental plastic strain

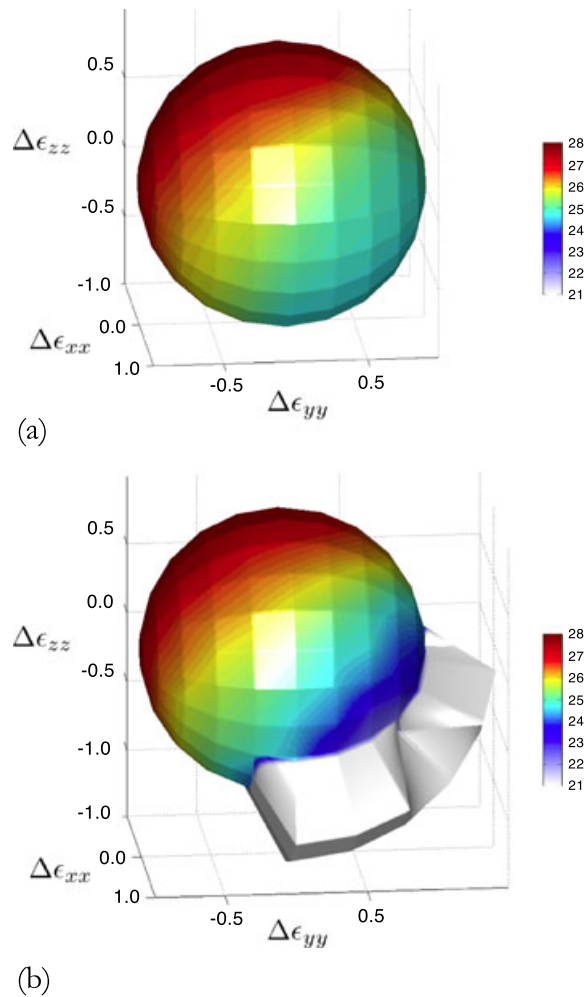


Figure 16. Localization function for combined vertical compression and lateral extension: (a) TS#63, (b) TS#64. Color bar is natural logarithm of \mathcal{F} . TS, Time Step.

response depends on the probe direction. The incremental plastic strain in the z -direction is negative for all the probes, implying that only probes that further compress the REV in the z -direction generate slips on the microfractures, whereas probes that pull the REV in the lateral direction only induce elastic deformation on the elements.

Figure 19 portrays the incremental von Mises stress responses to the strain probes at the end of TS#63 and TS#64. The magnitude of a probe vector represents the stress response (in megapascal) to a strain probe direction after a constant has been added, again, to prevent the introduction of negative values. The color contour shows the true value of the incremental von Mises stress. It can be observed that the von Mises stress increment is negative or only mildly positive even when the REV is loaded further in compression. This implies that further slips in the existing microfractures occur, resulting in a decrease in the overall REV stress response.

3.3. Scale effects

Because the AES technique smears the slip throughout the host finite element, the length of the microfracture is determined by the scale of the finite elements, that is, the coarser the mesh, the larger the finite elements, the greater is the extent of the microfracture. In addition, the rate of softening is determined by the characteristic distance ζ^+ in the sense that the shorter the sliding

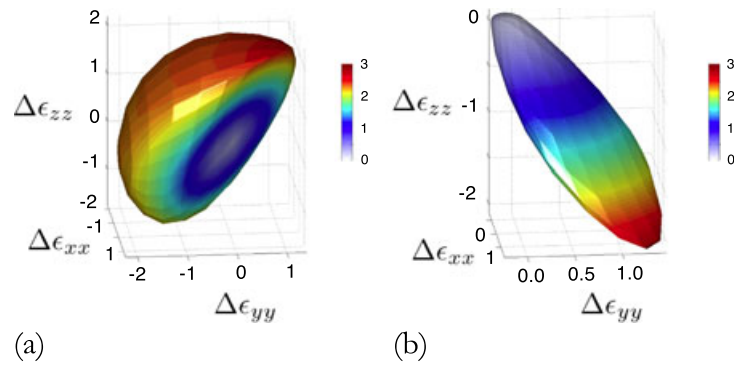


Figure 17. Strain increments for the representative elementary volume at TS#63: (a) elastic strain increment, and (b) plastic strain increment. Axes and color bars are multiplied by 10^{-6} . TS, Time Step.

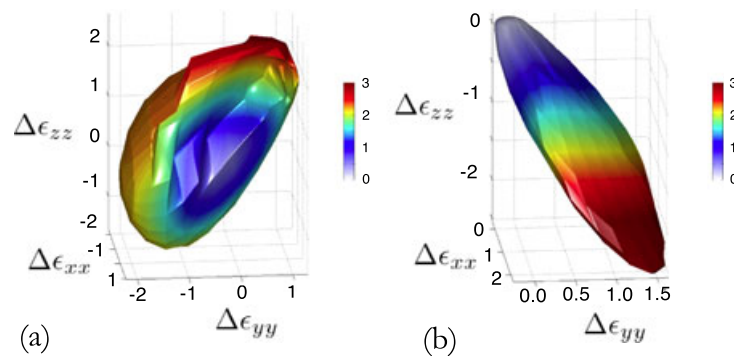


Figure 18. Strain increments for the representative elementary volume at TS#64: (a) elastic strain increment, and (b) plastic strain increment. Axes and color bars are multiplied by 10^{-6} . TS, Time Step.

distance, the faster the strength drop, the higher the softening modulus. This section reports the results of parametric studies investigating the impacts of microfracture scale and sliding distance on the overall mechanical response of microfractured porous rocks.

Figures 20 and 21 show the variation of the von Mises stress with time using two different mesh sizes for the shearing and extension loading and the combined compression and lateral extension loading simulations, respectively. The coarser mesh employs $4 \times 4 \times 4$ cubical elements, while the finer mesh employs $8 \times 8 \times 8$ cubical elements in the REV. A third simulation employs the finer mesh but with ζ^+ reduced by half, thereby increasing the softening modulus two times. Note that we have changed the microstructure of the REV from that shown in Figure 3 so we could embed identical pore configurations into the coarser and finer meshes. Hence, the results reported in this section may not be compared directly with those reported in Section 3.1.

With conforming finite elements, it is generally well known that the finer the mesh, the softer the response. This is due to the inability of the coarser mesh to capture higher-order deformation modes. However, Figures 20 and 21 demonstrate the effect of slip weakening on larger elements in the presence of microfractures, in which the coarser mesh induces a softer response of the REV. This results should not be interpreted as a sign of the lack of mesh objectivity of the finite element solution because of the following reason: It must be noted that the REV has pores, which establish a scale in the volume. In addition, the dimensions of the finite element establish the scale of the microfractures. As their relative scales change, so does the overall response of the volume. This reflects the effect of relative scales and not that of mesh sensitivity that is typically understood in classic finite element analysis, although the quality of the mesh also plays a role on the spatial resolution of the boundary value problem particularly with conforming elements that have not been enhanced.

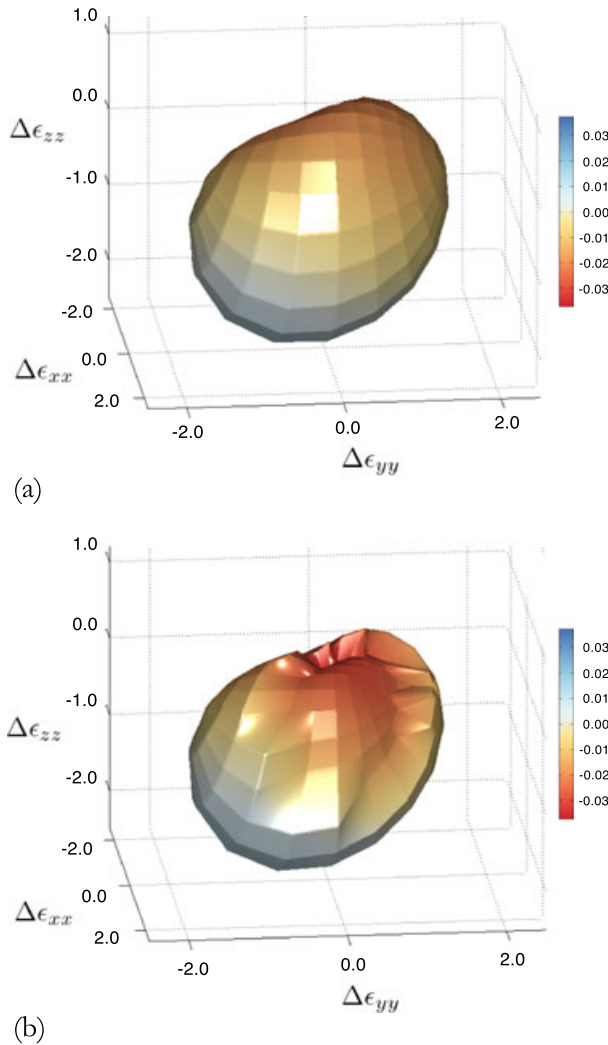


Figure 19. Incremental von Mises stress: (a) TS#63, (b) TS#64. Color bar in megapascal (MPa). TS, Time Step.

For the combined extension and shearing simulation with the finer mesh, the continuum response bifurcated into a shear band mode at TS#44, whereas the coarser mesh bifurcated a bit earlier at TS#36 because of the earlier onset of softening, as shown in Figure 20. A comparison of the unit normal vectors $\mathbf{n}_{\text{coarse}}$ and \mathbf{n}_{fine} at the two bifurcation points reveals that nearly the same shear band has formed, with

$$\mathbf{n}_{\text{coarse}} = \begin{Bmatrix} 0.42 \\ -0.57 \\ 0.70 \end{Bmatrix}, \quad \mathbf{n}_{\text{fine}} = \begin{Bmatrix} 0.46 \\ -0.61 \\ 0.64 \end{Bmatrix}.$$

However, with the coarse mesh simulation, an alternative shear band has also been detected to emerge at the same time step, with $\mathbf{n}_{\text{coarse}} = \{0.53, 0.34, 0.78\}$.

Reducing the characteristic distance ζ^+ further enhances softening, as portrayed by the results of the simulation where the sliding distance was reduced by 50%. This is to be expected because this parameter determines the rate of slip weakening and, hence, the value of the pore-scale softening modulus. As noted previously, ζ^+ is scale-dependent: the critical slip distance at nanoscale fractures is orders of magnitude smaller than the critical slip distance at kilometer-scale faults [73, 74]. One

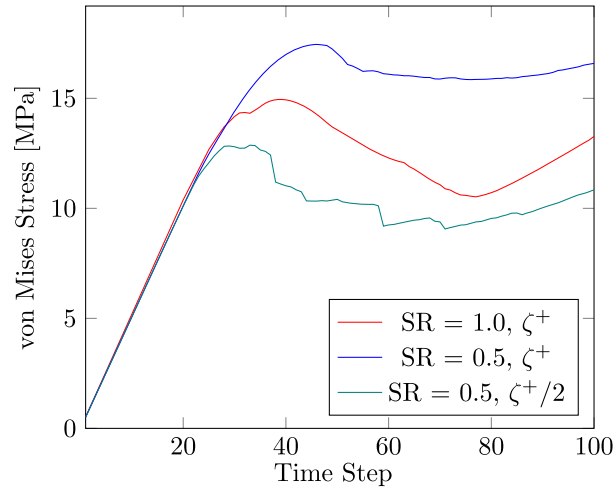


Figure 20. Variation of von Mises stress with time for the combined shearing and extension simulation. SR = ratio of microfracture scale to largest pore scale.

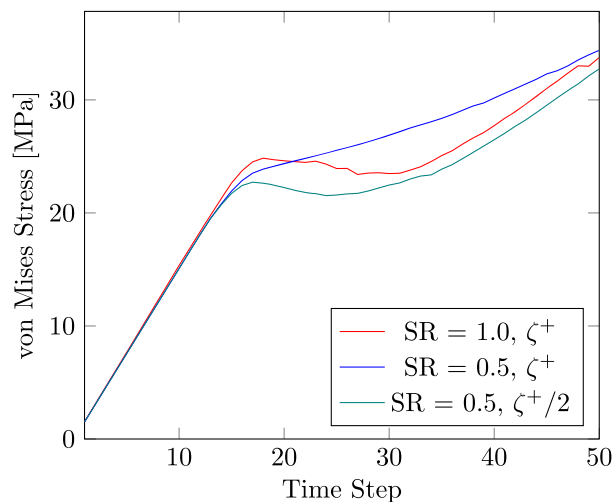


Figure 21. Variation of von Mises stress with time for the combined vertical compression and lateral extension simulation. SR = ratio of microfracture scale to largest pore scale.

can argue that this nanoscale parameter could be scaled from the overall softening response of the specimen-scale sample in much the same way that the slip weakening distance in a geologic fault could be scaled from the final slip of the fault [74], or from the rate of stress drop [73]. Current research is underway focusing on the aspect of scaling the critical slip distance of microfractures based on laboratory-scale specimen responses.

4. CONCLUSIONS

We have presented a computational framework for capturing the microfracture processes triggering shear band bifurcation in porous crystalline rocks. The framework combines a previously developed pore-scale mechanistic model with computational homogenization and continuum shear band bifurcation accommodating an incrementally nonlinear overall constitutive response. Whereas the cubical model and f.c.c. crystal representation may be considered as simplistic compared with the highly complex microstructure of real crystalline rocks, they accommodate the presence of pores

in the solid and the stress concentrations that develop in the edges and corners of the pores, which eventually lead to shear band bifurcation.

Results of numerical simulations suggest that single-mechanism elastoplasticity is insufficient to describe the incremental responses of rocks. The overall constitutive tangent operator of the REV has many branches depending on which fracture mechanisms activate, unlike the classic elastoplastic formulation that has only one loading branch. Thus, it is important to conduct strain probing to capture the multiple branches of the overall tangent constitutive operator and their impacts on shear band bifurcation. For the numerical examples considered in this paper, however, the stress state appears to have a more significant impact on the ensuing shear band orientation than the direction of the strain probes. While the strain probes could trigger different branches of the homogenized constitutive response, it appears that their effect on the orientation of the shear band is only second order.

The overall stress drop is more pronounced in a loading module that creates microfractures with predominantly interface separation as compared with that, which creates microfractures with predominant contact mode. This is because slip can occur more freely in a microfracture with interface separation, whereas it is more constrained when it has to overcome the frictional resistance in a contact mode.

The proposed computational framework fully recognizes the separation of scales: no attempt was made to link the microfractures within the REV with the overall macroscopic shear band. Instead, continuum bifurcation on the REV level is understood to signal the onset of a macroscopic shear band. In this case, finite element enhancements such as the extended finite element method or the AES technique may be used for the larger scale to delineate the propagation of the band at post-bifurcation.

APPENDIX

Interface separation. The following are the relevant stiffness terms for interface separation:

$$\begin{aligned}
 \mathbf{K}_{dd}^e &= \int_{V^e} \mathbf{B}_e^T \mathbf{D}^e \mathbf{B}_e dV, \\
 \mathbf{K}_{d\zeta_{t1}}^e &= \int_{V^e} \mathbf{B}_e^T \frac{\partial \sigma^e}{\partial \zeta_{t1}} dV = - \int_{V^e} \mathbf{B}_e^T \mathbf{D}^e (\nabla f_e^h \otimes \mathbf{m}_1)^s dV, \\
 \mathbf{K}_{d\zeta_{t2}}^e &= - \int_{V^e} \mathbf{B}_e^T \mathbf{D}^e (\nabla f_e^h \otimes \mathbf{m}_2)^s dV, \\
 \mathbf{K}_{d\zeta_n}^e &= - \int_{V^e} \mathbf{B}_e^T \mathbf{D}^e (\nabla f_e^h \otimes \mathbf{n})^s dV, \\
 \mathbf{K}_{\zeta_{t1}d}^e &= \frac{\partial f_{t1}^e}{\partial d^e}, & \mathbf{K}_{\zeta_{t1}\zeta_{t1}}^e &= \frac{\partial f_{t1}^e}{\partial \zeta_{t1}^e}, & \mathbf{K}_{\zeta_{t1}\zeta_{t2}}^e &= \frac{\partial f_{t1}^e}{\partial \zeta_{t2}^e}, \\
 \mathbf{K}_{\zeta_{t1}\zeta_n}^e &= \frac{\partial f_{t1}^e}{\partial \zeta_n^e}, & \mathbf{K}_{\zeta_{t2}d}^e &= \frac{\partial f_{t2}^e}{\partial d^e}, & \mathbf{K}_{\zeta_{t2}\zeta_{t1}}^e &= \frac{\partial f_{t2}^e}{\partial \zeta_{t1}^e}, \\
 \mathbf{K}_{\zeta_{t2}\zeta_{t2}}^e &= \frac{\partial f_{t2}^e}{\partial \zeta_{t2}^e}, & \mathbf{K}_{\zeta_{t2}\zeta_n}^e &= \frac{\partial f_{t2}^e}{\partial \zeta_n^e}, & \mathbf{K}_{\zeta_n d}^e &= \frac{\partial f_n^e}{\partial d^e}, \\
 \mathbf{K}_{\zeta_n\zeta_{t1}}^e &= \frac{\partial f_n^e}{\partial \zeta_{t1}^e}, & \mathbf{K}_{\zeta_n\zeta_{t2}}^e &= \frac{\partial f_n^e}{\partial \zeta_{t2}^e}, & \mathbf{K}_{\zeta_n\zeta_n}^e &= \frac{\partial f_n^e}{\partial \zeta_n^e},
 \end{aligned} \tag{A.1}$$

The derivatives of f_{t1}^e are as follows:

$$\begin{aligned}
 \frac{\partial f_{t1}^e}{\partial d^e} &= \frac{1}{V^e} \int_{V^e} \frac{\partial f_{t1}^e}{\partial \sigma^e} : \mathbf{D}^e : \mathbf{B}^e dV, \\
 &= \frac{1}{V^e} \int_{V^e} \text{sign}(\tau_1^e) (\mathbf{n} \otimes \mathbf{m}_1)^s : \mathbf{D}^e : \mathbf{B}^e dV
 \end{aligned} \tag{A.2}$$

and

$$\frac{\partial f_{t1}^e}{\partial \zeta_{t1}^e} = \text{sign}(\tau_1^e) (\mathbf{n} \otimes \mathbf{m}_1)^s : \frac{\partial \boldsymbol{\sigma}^e}{\partial \zeta_{t1}^e} - \frac{\partial c_1^e}{\partial \zeta_{t1}^e}, \quad (\text{A.3})$$

where

$$\frac{\partial c_1^e}{\partial \zeta_{t1}^e} = \begin{cases} -\text{sign}(\zeta_{t1}^e) \frac{\tau_{0,1}^e}{\zeta_{t1}^+} & \text{if } 0 \leq \|\zeta_{t1}^e\| \leq \zeta_{t1}^+, \\ 0 & \text{if } \|\zeta_{t1}^e\| > \zeta_{t1}^+, \end{cases} \quad (\text{A.4})$$

$$\frac{\partial \boldsymbol{\sigma}^e}{\partial \zeta_{t1}^e} = -\mathbf{D}^e : \frac{1}{V^e} \int_{V^e} (\nabla f^h \otimes \mathbf{m}_1)^s dV. \quad (\text{A.5})$$

The remaining derivatives of f_{t1}^e are as follows:

$$\frac{\partial f_{t1}^e}{\partial \zeta_{t2}^e} = \text{sign}(\tau_1^e) (\mathbf{n} \otimes \mathbf{m}_1)^s : \frac{\partial \boldsymbol{\sigma}^e}{\partial \zeta_{t2}^e}, \quad (\text{A.6})$$

where

$$\frac{\partial \boldsymbol{\sigma}^e}{\partial \zeta_{t2}^e} = -\mathbf{D}^e : \frac{1}{V^e} \int_{V^e} (\nabla f^h \otimes \mathbf{m}_2)^s dV; \quad (\text{A.7})$$

and

$$\frac{\partial f_{t1}^e}{\partial \zeta_n^e} = (\mathbf{n} \otimes \mathbf{m}_1)^s : \frac{\partial \boldsymbol{\sigma}^e}{\partial \zeta_n^e}, \quad (\text{A.8})$$

where

$$\frac{\partial \boldsymbol{\sigma}^e}{\partial \zeta_n^e} = -\mathbf{D}^e : \frac{1}{V^e} \int_{V^e} (\nabla f^h \otimes \mathbf{n})^s dV. \quad (\text{A.9})$$

The derivatives of f_{t2}^e are as follows:

$$\begin{aligned} \frac{\partial f_{t2}^e}{\partial \mathbf{d}^e} &= \frac{1}{V^e} \int_{V^e} \frac{\partial f_{t2}^e}{\partial \boldsymbol{\sigma}^e} : \mathbf{D}^e : \mathbf{B}^e dV, \\ &= \frac{1}{V^e} \int_{V^e} \text{sign}(\tau_2^e) (\mathbf{n} \otimes \mathbf{m}_2)^s : \mathbf{D}^e : \mathbf{B}^e dV, \end{aligned} \quad (\text{A.10})$$

$$\frac{\partial f_{t2}^e}{\partial \zeta_{t1}^e} = \text{sign}(\tau_2^e) (\mathbf{n} \otimes \mathbf{m}_2)^s : \frac{\partial \boldsymbol{\sigma}^e}{\partial \zeta_{t1}^e}, \quad (\text{A.11})$$

$$\frac{\partial f_{t2}^e}{\partial \zeta_{t2}^e} = \text{sign}(\tau_2^e) (\mathbf{n} \otimes \mathbf{m}_2)^s : \frac{\partial \boldsymbol{\sigma}^e}{\partial \zeta_{t2}^e} - \frac{\partial c_2^e}{\partial \zeta_{t2}^e}, \quad (\text{A.12})$$

and

$$\frac{\partial f_{t2}^e}{\partial \zeta_n^e} = (\mathbf{n} \otimes \mathbf{m}_2)^s : \frac{\partial \boldsymbol{\sigma}^e}{\partial \zeta_n^e}, \quad (\text{A.13})$$

where

$$\frac{\partial c_2^e}{\partial \zeta_{t2}^e} = \begin{cases} -\text{sign}(\zeta_{t2}^e) \frac{\tau_{0,2}^e}{\zeta_{t2}^+} & \text{if } 0 \leq \|\zeta_{t2}^e\| \leq \zeta_{t2}^+, \\ 0 & \text{if } \|\zeta_{t2}^e\| > \zeta_{t2}^+, \end{cases} \quad (\text{A.14})$$

The derivatives of f_n^e are as follows:

$$\begin{aligned} \frac{\partial f_n^e}{\partial \mathbf{d}^e} &= \frac{1}{V^e} \int_{V^e} \frac{\partial f_n^e}{\partial \boldsymbol{\sigma}^e} : \mathbf{D}^e : \mathbf{B}^e \, dV, \\ &= \frac{1}{V^e} \int_{V^e} (\mathbf{n} \otimes \mathbf{n}) : \mathbf{D}^e : \mathbf{B}^e \, dV, \end{aligned} \tag{A.15}$$

$$\begin{aligned} \frac{\partial f_n^e}{\partial \zeta_{t1}^e} &= (\mathbf{n} \otimes \mathbf{n}) : \frac{\partial \boldsymbol{\sigma}^e}{\partial \zeta_{t1}^e}, \\ &= (\mathbf{n} \otimes \mathbf{n}) : \left(-\mathbf{D}^e : \frac{1}{V} \int_{V^e} (\nabla f^h \otimes \mathbf{m}_1)^s \, dV \right), \end{aligned} \tag{A.16}$$

$$\begin{aligned} \frac{\partial f_n^e}{\partial \zeta_{t2}^e} &= (\mathbf{n} \otimes \mathbf{n}) : \frac{\partial \boldsymbol{\sigma}^e}{\partial \zeta_{t2}^e}, \\ &= (\mathbf{n} \otimes \mathbf{n}) : \left(-\mathbf{D}^e : \frac{1}{V} \int_{V^e} (\nabla f^h \otimes \mathbf{m}_2)^s \, dV \right), \end{aligned} \tag{A.17}$$

and

$$\frac{\partial f_n^e}{\partial \zeta_n^e} = (\mathbf{n} \otimes \mathbf{n}) : \frac{\partial \boldsymbol{\sigma}^e}{\partial \zeta_n^e} - \frac{\partial b^e}{\partial \zeta_n^e}, \tag{A.18}$$

where

$$\frac{\partial b^e}{\partial \zeta_n^e} = \begin{cases} -\frac{\sigma_0^e}{\zeta_n^+} & \text{if } 0 \leq \zeta_n^e \leq \zeta_n^+, \\ 0 & \text{if } \zeta_n^e > \zeta_n^+, \end{cases} \tag{A.19}$$

Interface contact. The following are the relevant stiffness terms for interface contact:

$$\begin{aligned} \mathbf{K}_{dd}^e &= \int_{V^e} \mathbf{B}_e^T \mathbf{D}^e \mathbf{B}_e \, dV, \\ \mathbf{K}_{d\zeta_t}^e &= - \int_{V^e} \mathbf{B}_e^T \mathbf{D}^e (\nabla f_e^h \otimes \mathbf{m})^s \, dV, \\ \mathbf{K}_{\zeta_t d}^e &= \frac{\partial f_t^e}{\partial \mathbf{d}^e}, \quad \mathbf{K}_{\zeta_t \zeta_t}^e = \frac{\partial f_t^e}{\partial \zeta_t^e}. \end{aligned} \tag{A.20}$$

The derivatives of f_t^e are as follows:

$$\begin{aligned} \frac{\partial f_t^e}{\partial \mathbf{d}^e} &= \frac{1}{V^e} \int_{V^e} \frac{\partial f_t^e}{\partial \boldsymbol{\sigma}^e} : \mathbf{D}^e : \mathbf{B}^e \, dV, \\ &= \frac{1}{V^e} \int_{V^e} \text{sign}(\tau^e) [(\mathbf{n} \otimes \mathbf{m})^s + \mu^e (\mathbf{n} \otimes \mathbf{n})] : \mathbf{D}^e : \mathbf{B}^e \, dV, \end{aligned} \tag{A.21}$$

and

$$\begin{aligned} \frac{\partial f_t^e}{\partial \zeta_t^e} &= \text{sign}(\tau^e) [(\mathbf{n} \otimes \mathbf{m})^s + \mu^e (\mathbf{n} \otimes \mathbf{n})] : \frac{\partial \boldsymbol{\sigma}^e}{\partial \zeta_t^e} \\ &\quad + \frac{\partial \mu^e}{\partial \zeta_t^e} \sigma^e - \frac{\partial c^e}{\partial \zeta_t^e}, \end{aligned} \tag{A.22}$$

where

$$\frac{\partial c^e}{\partial \zeta_t^e} = \begin{cases} -\text{sign}(\zeta_t^e) \frac{\tau_0^e}{\zeta_t^+} & \text{if } 0 \leq \|\zeta_t^e\| \leq \zeta_t^+, \\ 0 & \text{if } \|\zeta_t^e\| > \zeta_t^+, \end{cases} \tag{A.23}$$

$$\frac{\partial \mu^e}{\partial \zeta_t^e} = \begin{cases} \text{sign}(\zeta_t^e) \frac{\bar{\mu}}{\zeta_t^+} & \text{if } 0 \leq \|\zeta_t^e\| \leq \zeta_t^+, \\ 0 & \text{if } \|\zeta_t^e\| > \zeta_t^+, \end{cases} \quad (\text{A.24})$$

$$\frac{\partial \sigma^e}{\partial \zeta_t^e} = -\mathbf{D}^e : \frac{1}{V} \int_{V^e} (\nabla f^h \otimes \mathbf{m})^s dV, \quad (\text{A.25})$$

ACKNOWLEDGEMENTS

This material is based upon work supported by the US Department of Energy, Office of Science, Office of Basic Energy Sciences, Geosciences Research Program, under Award Number DE-FG02-03ER15454; and by the National Science Foundation under Award Number CMMI-1462231. The first author is grateful for a Stanford Graduate Fellowship and a John A. Blume Fellowship that provided partial support for his PhD studies at Stanford. We thank the two anonymous reviewers for their constructive reviews.

REFERENCES

1. Borja RI, Aydin A. Computational modeling of deformation bands in granular media, I: geological and mathematical framework. *Computer Methods in Applied Mechanics and Engineering* 2004; **193**:2667–2698.
2. Borja RI. Computational modeling of deformation bands in granular media, II: numerical simulations. *Computer Methods in Applied Mechanics and Engineering* 2004; **193**:2699–2718.
3. Rudnicki JW, Rice JR. Conditions for the localization of deformation in pressure-sensitive dilatant materials. *Journal of the Mechanics and Physics of Solids* 1975; **23**:371–394.
4. Baud P, Schubnel A, Wong TF. Dilatancy, compaction and failure mode in Solnhofen limestone. *Journal of Geophysical Research* 2000; **195**:19289–19303.
5. Vajdova V, Zhu W, Chen TMN, Wong TF. Micromechanics of brittle faulting and cataclastic flow in Tavel limestone. *Journal of Structural Geology* 2010; **32**:1158–1169.
6. Vajdova V, Baud P, Wu L, Wong TF. Micromechanics of inelastic compaction in two allochemical limestones. *Journal of Structural Geology* 2012; **43**:100–117.
7. Wang B, Chen Y, Wong TF. A discrete element model for the development of compaction localization in granular rock. *Journal of Geophysical Research* 2008; **113**:B03202.
8. Borja RI, Andrade JE. Critical state plasticity. Part VI: Meso-scale finite element simulation of strain localization in discrete granular materials. *Computer Methods in Applied Mechanics and Engineering* 2006; **195**:5115–5140.
9. Borja RI, Song X, Rechenmacher A, Abedi S, Wu W. Shear band in sand with spatially varying density. *Journal of the Mechanics and Physics of Solids* 2013; **61**:219–234.
10. Borja RI, Song X, Wu W. Critical state plasticity, Part VII: triggering a shear band in variably saturated porous media. *Computer Methods in Applied Mechanics and Engineering* 2013; **261–262**:66–82.
11. Guo N, Zhao J. A coupled FEM/DEM approach for hierarchical multiscale modelling of granular media. *International Journal for Numerical Methods in Engineering* 2014; **99**:789–818.
12. Li X, Konietzky H. Numerical simulation schemes for time-dependent crack growth in hard brittle rock. *Acta Geotechnica* 2015; **10**:513–531.
13. Lin J, Wu W, Borja RI. Micropolar hypoplasticity for persistent shear band in heterogeneous granular materials. *Computer Methods in Applied Mechanics and Engineering* 2015; **289**:24–43.
14. Liu Y, Filonova V, Hu N, Yuan Z, Fish J, Yuan Z, Belytschko T. A regularized phenomenological multiscale damage model. *International Journal for Numerical Methods in Engineering* 2014; **99**:867–887.
15. Song X, Borja RI. Mathematical framework for unsaturated flow in the finite deformation range. *International Journal for Numerical Methods in Engineering* 2014; **37**:658–682.
16. Song X, Borja RI. Finite deformation and fluid flow in unsaturated soils with random heterogeneity. *Vadose Zone Journal* 2014; **13**(5). Doi:10.2136/vzj2013.07.0131.
17. Behnia M, Goshdashti K, Marji MF, Golshani A. Numerical simulation of interaction between hydraulic and natural fractures in discontinuous media. *Acta Geotechnica* 2015; **10**:533–546.
18. Bennett KC, Berla LA, Nix WD, Borja RI. Instrumented nanoindentation and 3D mechanistic modeling of a shale at multiple scales. *Acta Geotechnica* 2015; **10**:1–14.
19. Catalano E, Chareyre B, Barthélémy E. Pore-scale modeling of fluid-particles interaction and emerging poromechanical effects. *International Journal for Numerical and Analytical Methods in Geomechanics* 2014; **38**: 51–71.
20. Foster CD, Nejad TM. Embedded discontinuity finite element modeling of fluid flow in fractured porous media. *Acta Geotechnica* 2013; **8**:49–57.

21. Fu P, Johnson SM, Carrigan C. An explicitly coupled hydrogeomechanical model for simulating hydraulic fracturing in arbitrary discrete fracture networks. *International Journal for Numerical and Analytical Methods in Geomechanics* 2013; **37**:2278–2300.
22. Ganzer L, Reitenbach V, Pudlo D, Albrecht D, Singhe AT, Awemo KN, Wienand J, Gaupp R. Experimental and numerical investigations on CO₂ injection and enhanced gas recovery effects in Altmark gas field (Central Germany). *Acta Geotechnica* 2014; **9**:39–47.
23. Gou Y, Hou Z, Liu H, Zhou L, Were P. Numerical simulation of carbon dioxide injection for enhanced gas recovery (CO₂-EGR) in Altmark natural gas field. *Acta Geotechnica* 2014; **9**:49–58.
24. Jourdain X, Colliat JB, De Sa C, Benboudjema F, Gatuingt F. Upscaling permeability for fractured concrete: meso-macro numerical approach coupled to strong discontinuities. *International Journal for Numerical and Analytical Methods in Geomechanics* 2014; **38**:536–550.
25. Katsuki D, Gutierrez M, Almrabat A. Stress-dependent elastic wave velocity of microfractured sandstone. *International Journal for Numerical and Analytical Methods in Geomechanics* 2014; **38**:441–456.
26. Li L, Meng Q, Wang S, Li G, Tang C. A numerical investigation of the hydraulic fracturing behaviour of conglomerate in Glutenite formation. *Acta Geotechnica* 2013; **8**:597–618.
27. Sarris E, Papanastasiou P. Numerical modeling of fluid-driven fractures in cohesive poroelastoplastic continuum. *International Journal for Numerical and Analytical Methods in Geomechanics* 2013; **37**:1822–1846.
28. Xu T, Xu Q, Tang C, Ranjith PG. The evolution of rock failure with discontinuities due to shear creep. *Acta Geotechnica* 2013; **8**:567–581.
29. Mowar S, Zaman M, Stearns DW, Roegiers JC. Micro-mechanisms of pore collapse in limestone. *Journal of Petroleum Science and Engineering* 1996; **15**:221–235.
30. Tjioe M, Borja RI. On the pore-scale mechanisms leading to brittle and ductile deformation behavior of crystalline rocks. *International Journal for Numerical and Analytical Methods in Geomechanics* 2015; **39**:1165–1187.
31. Borja RI. *Plasticity Modeling and Computation*. Springer-Verlag: Berlin-Heidelberg, 2013.
32. Calvetti F, Tamagnini C, Viggiani G. On the incremental behaviour of granular soils. In *Numerical Models in Geomechanics*, Pande GN, Pietruszczak S (eds). Rotterdam: Balkema, 2002; 3–10.
33. Calvetti F, Viggiani G, Tamagnini C. A numerical investigation of the incremental behavior of granular soils. *Rivista Italiana di Geotecnica* 2003; **37**:11–29.
34. Desrues J, Chambon R. Shear band analysis for granular materials: the question of incremental non-linearity. *Ingenieur-Archiv* 1989; **59**:187–196.
35. Anandarajah A, Khaled S, Kuganenthira N. Incremental stress-strain behavior of granular soil. *ASCE Journal of Geotechnical Engineering* 1995; **121**(1):57–67.
36. Royis P, Doanh T. Theoretical analysis of strain response envelopes using incrementally non-linear constitutive equations. *International Journal for Numerical and Analytical Methods in Geomechanics* 1998; **22**:97–132.
37. He X, Xu C. Discrete element modelling of rock cutting: from ductile to brittle transition. *International Journal for Numerical and Analytical Methods in Geomechanics* 2015; **39**:1331–1351.
38. Jiang M, Zhang F, Thornton C. A simple three-dimensional distinct element modeling of the mechanical behavior of bonded sands. *International Journal for Numerical and Analytical Methods in Geomechanics* 2015; **39**:1791–1820.
39. Bardet JP. Numerical simulations of the incremental responses of idealized granular materials. *International Journal of Plasticity* 1994; **10**(8):879–908.
40. Kishino Y. On the incremental nonlinearity observed in a numerical model for granular media. *Rivista Italiana di Geotecnica* 2002; **3**:30–38.
41. Alonso-Marroquín F, Herrmann HJ. The incremental response of soils: an investigation using a discrete-element model. *Journal of Engineering Mathematics* 2005; **52**:11–34.
42. Froio F, Roux JN. Incremental response of a model granular material by stress probing with DEM simulations. *AIP Conference Proceedings*, 1227, 2010; 183–197. DOI:<http://dx.doi.org/10.1063/1.3435388>.
43. Andrade JE, Lim KW, Avila CF, Vlahinić I. Granular element method for computational particle mechanics. *Computer Methods in Applied Mechanics and Engineering* 2012; **241–244**:262–274.
44. Dujc J, Brank B, Ibrahimbegovic A. Stress-hybrid quadrilateral finite element with embedded strong discontinuity for failure analysis of plane stress solids. *International Journal for Numerical Methods in Engineering* 2013; **94**:1075–1098.
45. Karoui A, Mansouti K, Renard Y, Arfaoui M. The extended finite element method for cracked hyperelastic materials: A convergence study. *International Journal for Numerical Methods in Engineering* 2014; **100**:222–242.
46. Sadaba S, Romero I, Gonzalez C, Llorca J. A stable X-FEM in cohesive transition from closed to open crack. *International Journal for Numerical Methods in Engineering* 2014; **101**:540–570.
47. Saksala T, Brancherie D, Harari I, Ibrahimbegovic A. Combined continuum damage-embedded discontinuity model for explicit dynamic fracture analyses of quasi-brittle materials. *International Journal for Numerical Methods in Engineering* 2015; **101**:230–250.
48. Sun H, Waisman H, Betti R. A multiscale flaw detection algorithm based on XFEM. *International Journal for Numerical Methods in Engineering* 2014; **100**:477–503.
49. Miehe C, Koch A. Computational micro-to-macro transitions of discretized microstructures undergoing small strains. *Archive of Applied Mechanics* 2002; **72**:300–317.
50. Borja RI, Wren JR. Discrete micromechanics of elastoplastic crystals. *International Journal for Numerical Methods in Engineering* 1993; **36**:3815–3840.

51. Borja RI, Rahmani H. Computational aspects of elasto-plastic deformation in polycrystalline solids. *Journal of Applied Mechanics* 2012; **79**:031024.
52. Borja RI, Rahmani H. Discrete micromechanics of elastoplastic crystals in the finite deformation range. *Computer Methods in Applied Mechanics and Engineering* 2014; **275**:234–263.
53. Armero F, Garikipati K. An analysis of strong discontinuities in multiplicative finite strain plasticity and their relation with the numerical simulation of strain localization in solids. *International Journal of Solids and Structures* 1996; **33**:2863–2885.
54. Borja RI. A finite element model for strain localization analysis of strongly discontinuous fields based on standard Galerkin approximations. *Computer Methods in Applied Mechanics and Engineering* 2000; **190**:1529–1549.
55. Borja RI, Regueiro RA. Strain localization of frictional materials exhibiting displacement jumps. *Computer Methods in Applied Mechanics and Engineering* 2001; **190**:2555–2580.
56. Gupta P, Duarte CA. Simulation of non-planar three-dimensional hydraulic fracture propagation. *International Journal for Numerical and Analytical Methods in Geomechanics* 2014; **38**:1397–1430.
57. Haghghat E, Pietruszczak S. On modeling of discrete propagation of localized damage in cohesive–frictional materials. *International Journal for Numerical and Analytical Methods in Geomechanics* 2015; **39**:1774–1790.
58. Linder C, Raina A. A strong discontinuity approach on multiple levels to model solids at failure. *Computer Methods in Applied Mechanics and Engineering* 2013; **253**:558–583.
59. Linder C, Zhang X. A marching cubes based failure surface propagation concept for three-dimensional finite elements with non-planar embedded strong discontinuities of higher-order kinematics. *International Journal for Numerical Methods in Engineering* 2013; **96**:339–372.
60. Linder C, Zhang X. Three-dimensional finite elements with embedded strong discontinuities to model failure in electromechanical coupled materials. *Computer Methods in Applied Mechanics and Engineering* 2014; **273**:143–160.
61. Mosler J, Meschke G. 3D modeling of strong discontinuities in elastoplastic solids: fixed and rotating localization formulations. *International Journal for Numerical Methods in Engineering* 2003; **57**:1553–1576.
62. Oliver J, Huespe AE. Continuum approach to material failure in strong discontinuity settings. *Computer Methods in Applied Mechanics and Engineering* 2004; **193**:3195–3220.
63. Pouya A. Micro-macro approach for the rock salt behaviour. *European Journal of Mechanics - A/Solids* 2000; **19**:1015–1028.
64. Simo JC, Oliver J. A new approach to the analysis and simulation of strain softening in solids. In *Fracture and Damage in Quasibrittle Structures*, Bazant ZP, Bittnar Z, Jirásek M, Mazars J (eds). E&FN Spon: London, 1994; 25–39.
65. Borja RI. Assumed enhanced strain and the extended finite element methods: a unification of concepts. *Computer Methods in Applied Mechanics and Engineering* 2008; **197**:2789–2803.
66. Hughes TJR. *The Finite Element Method*. Prentice-Hall: New Jersey, 1987.
67. Runesson K, Peric D, Sture S. Discontinuous bifurcations of elastic-plastic solutions at plane stress and plane strain. *International Journal of Plasticity* 1991; **7**:99–121.
68. Ortiz M, Leroy Y, Needleman A. A finite element method for localized failure analysis. *Computer Methods in Applied Mechanics and Engineering* 1987; **61**:189–214.
69. Andrade JE, Borja RI. Capturing strain localization in dense sands with random density. *International Journal for Numerical Methods in Engineering* 2006; **67**:1531–1564.
70. Leroy Y, Ortiz M. Localization analysis under dynamic loading. *Institute of Physics Conference Series* 1989; **102**:257–265.
71. Oliver J, Huespe AE, Cante JC, Díaz G. On the numerical resolution of the discontinuous material bifurcation problem. *International Journal for Numerical Methods in Engineering* 2010; **83**:786–804.
72. Wong TF. Shear fracture energy of Westerly granite from post-failure behavior. *Journal of Geophysical Research: Solid Earth* 1982; **87**:990–1000.
73. Fukuyama E, Mikumo T, Olsen KB. Estimation of the critical slip-weakening distance: Theoretical background. *Bulletin of the Seismological Society of America*; **93**:1835–1840.
74. Cocco M, Tinti E, Marone C, Piatanesi A. Chapter 7 Scaling of Slip Weakening Distance with Final Slip during Dynamic Earthquake Rupture. In *Fault-Zone Properties and Earthquake Rupture Dynamics*, Vol. 74, Fukuyama E (ed.). International Geophysics, Academic Press Inc., 2009; 163–186.